

AD-A172 375

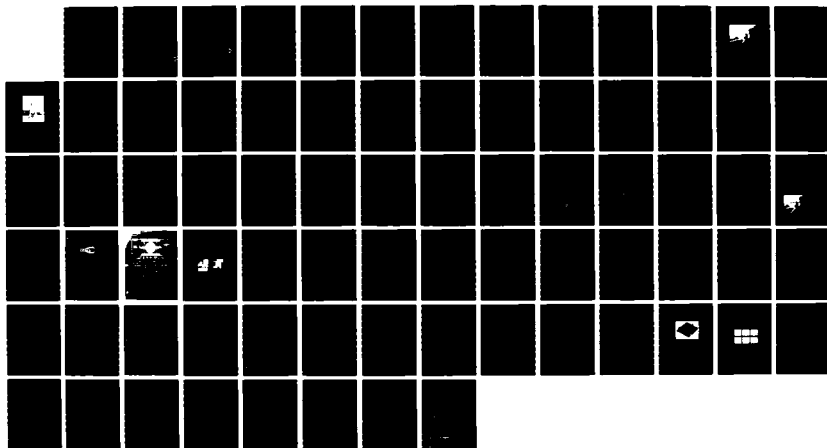
INVESTIGATION OF MAGNETOSTATIC SURFACE WAVES FOR
ANISOTROPIC EFFECTS(U) AIR FORCE INST OF TECH
WRIGHT-PATTERSON AFB OH SCHOOL OF ENGINEERING
R E FLOYD JUN 86 AFIT/GE/ENG/86J-1

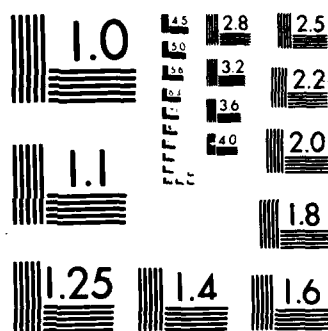
1/1

UNCLASSIFIED

F/G 20/3

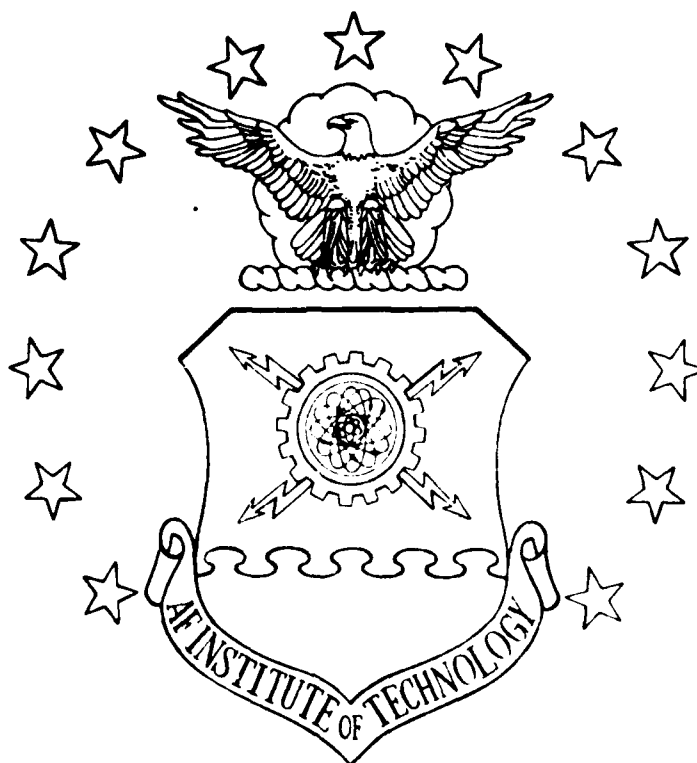
NL





1

AD-A172 375



DTIC FILE COPY

INVESTIGATION OF MAGNETOSTATIC
SURFACE WAVES FOR
ANISOTROPIC EFFECTS

THESIS

Robert E. Floyd
Captain, USAF
AFIT/GE/ENG/86J-1

DISTRIBUTION STATEMENT A

Approved for public release
Distribution Unlimited

DTIC
EFFECTIVE
OCT 2 1986

DEPARTMENT OF THE AIR FORCE
AIR UNIVERSITY

AIR FORCE INSTITUTE OF TECHNOLOGY

Wright-Patterson Air Force Base, Ohio

86 10 2

AFIT/GE/ENG/86J-1

INVESTIGATION OF MAGNETOSTATIC
SURFACE WAVES FOR
ANISOTROPIC EFFECTS

THESIS

Robert E. Floyd
Captain, USAF
AFIT/GE/ENG/86J-1

DTIC
ELECTE
OCT 2 1986
B

Approved for public release; distribution unlimited

AFIT/GE/ENG/86J-1

Investigation of Magnetostatic Surface Waves
For Anisotropic Effects

Thesis

Presented to the Faculty of the School of Engineering
of the Air Force Institute of Technology

Air University (AU)

In Partial Fulfillment of the
Requirements for the Degree

Master of Science in Electrical Engineering

Robert E. Floyd
Captain, USAF

June 1986

Approved for public release, distribution unlimited

Preface

The purpose of this thesis was to study the propagation of magnetostatic waves on a YIG ring. This topic was chosen because of my interests in experimentally oriented research and magnetostatics. I saw the opportunity to expand on someone's initial effort, with ideas and techniques of my own. This thesis topic provided me the chance to actually build electronic devices and test them. I believe the following findings and conclusions will be useful for those participating in research in the magnetostatic wave area.

I am most deeply grateful to Mr. James Sethares of the Rome Air Development Center's Electromagnetic Sciences Division for sponsoring the thesis, in providing samples for testing, advice during experimentation, and mostly his encouragement and guidance during my first years as a scientist and engineer.

A word of thanks also goes to Marc Calcaterra of the Avionics Laboratory at Wright-Patterson AFB for his help during the early experiments. Finally, I am extremely thankful for the continuing patience and assistance of my faculty advisor, Capt. Roger Colvin.

Robert E. Floyd

Table of Contents

	Page
Preface	ii
List of Figures	iv
Abstract	vi
I. Introduction	1
Background	1
Problem Statement and Scope	3
Overview	6
II. Magnetostatic Surface Wave Theory	8
Background	8
Magnetostatic Surface Waves	11
Crystallography	26
III. Experimental Apparatus and Procedures	31
Sample and Probes	31
Experimental Setup	35
Pulse Measurements	36
Delay Line Oscillator	38
IV. Experimental Results and Findings	40
Pulse Measurements	40
Delay Line Oscillator Measurements	46
V. Beam Steering	54
VI. Conclusions and Recommendations	60
Bibliography	64
Vita	66

DD1473



Accession For	
NTIS	SEARCH
DTIC	TAB
Unpublished	
Justified	
By	
DTIC	
Ac	
Dis	
A-1	

List of Figures

Figure		Page
1.1	YIG film on a ring	3
1.2	Top view of apparatus used in investigation	5
2.1	One spin-system	9
2.2	Geometry of the MSSW system	12
2.3	Dispersion relation for MSSW	27
2.4	Examples of low index planes	28
2.5	Example of crystalline direction	28
2.6	Top view of YIG single crystal	29
3.1	Diagram of YIG film used for rotation rate sensing	32
3.2	Cross-sectional view of Poturalski probe	34
3.3	Orientation of disc to rotation angle.	35
3.4	Test apparatus	36
3.5	Circuit diagram for pulse measurements	38
3.6	Circuit diagram for delay line oscillator	39
4.1	Amplitude distribution of MSW beam	40
4.2	Profiles of magnetostatic surface wave	41
4.3	Pulse measurements of sample one	43
4.4	Pulse measurements of sample two	44
4.5	Autocorrelation of random test file.	45
4.6	Autocorrelation sample one and two	47
4.7	Autocorrelation of insertion loss, group delay, and group velocity.	48

	Page
4.8 Block diagram of the delay line oscillator .	49
4.9 Frequency shifts versus rotation angle . . .	51
4.10 Autocorrelations of Figure 4.9 data.	52
4.11 Cross correlations of Figure 4.9 data.	53
5.1 Beam steering as a function of frequency . .	54
5.2 View of non-parallel RF shield	55
5.3 Regions of oblique incidence	56
5.4 Diagram of oblique incidence	57
5.5 Test apparatus for examining beam steering .	58
5.6 Separation of pulse with differing CW frequencies	59

Abstract

A unique test apparatus was designed in order to investigate the effect of launching magnetostatic surface waves at different angles on a yttrium-iron-garnet (YIG) single crystal film. Many characteristics of the magnetostatic waves were measured, including amplitude, time delay, and beam steering. There was slight dependence of these characteristics on the launch angle. A second, more sensitive technique using the YIG films as delay lines in an oscillating circuit, was found to verify the influence of magnetocrystalline anisotropy on the magnetostatic surface wave. A calculated shift in frequency of the oscillator was found to be in agreement with previous calculations and measurements of anisotropic constants.

In addition to these findings, an investigation of the influence of a metallization spaced closely to the propagation path was performed due to its influence on the above measurements. This metallization altered the velocity of the magnetostatic wave and demonstrated, for the first time, the refraction of a magnetostatic wave. This technique may prove useful for instantaneous frequency selection in electronic countermeasure equipment.

I. Introduction

Background

The work of Damon and Esbach in the late 1950's and early 1960's provides the theory on which much of magneto-static wave technology is based (Damon, 1960). Their derivations show the existence of magnetostatic surface wave modes in ferromagnetic materials. This behavior is similar to spin-wave propagation in an infinite media when no boundaries exist. With the introduction of boundaries, and as the excitation frequency is increased, the spin-wave behavior changes from one that is distributed throughout the volume of the medium, to one that is confined to the surface. Analysis indicates that these two types of modes are unique, frequency-dependent solutions to Maxwell's equations, and the equation of motion of the slab's magnetization (Damon, 1960:309). Surface wave propagation is initiated by external RF magnetic fields. The energy of the surface mode is concentrated along the surface where propagation takes place, with the propagation direction orthogonal to an applied DC field.

In 1968, experiments by Brundle and Freeman verified some of Damon and Esbach's theory. Brundle and Freeman were able to excite the surface wave mode on a thin, single crystal, yttrium-iron-garnet (YIG) slab where the magneto-static surface wavelengths were much smaller than the slab dimensions (Brundle, 1968). Results closely agreed with

Damon and Esbach's theory in terms of time delay, propagation direction, and dispersion. The surface wave was observed to be dispersive, and the wave velocity decreased as the excitation frequency was increased (Brundle, 1968:427).

Many signal processing applications have been developed using magnetostatic surface wave (MSSW) technology. Tunable microwave oscillators (Miller, 1976) and variable delay lines operating in the microwave spectrum have been developed. Many are based upon the theory of Damon and Esbach, the experiments of Brundle and Freeman, and others (Collins, 1977). This list of devices should also include the proposal of Newburgh, Blacksmith, Budreau, and Sethares of the Air Force Cambridge Research Laboratory (Newburgh, 1974). These researchers proposed the development of a small, highly sensitive and lightweight, non-inertial rotation rate sensor using MSSW propagation. Using an interferometric sensing scheme, the rotation rate would be detected by measuring the phase shifts of magnetostatic surface waves on a rotating YIG ring. In 1974, Sethares showed that MSSW propagation indeed could be achieved on a YIG thin film ring grown on a gadolinium-gallium-garnet (GGG) substrate (Sethares, 1975) (see Figure 1.1). The use of the thin film ring as a rotation sensor proved questionable because the experimental results exhibited large variations in coupling efficiency as the ring was rotated about its axis. Attributing the results to imperfections of the growth in the thin YIG film, Sethares

suggested the use of a thick film ring. This ring would be machined from a single crystal YIG boule, so that the crystalline imperfections, which occur during the liquid phase epitaxial growth process of a thin film, could be eliminated.

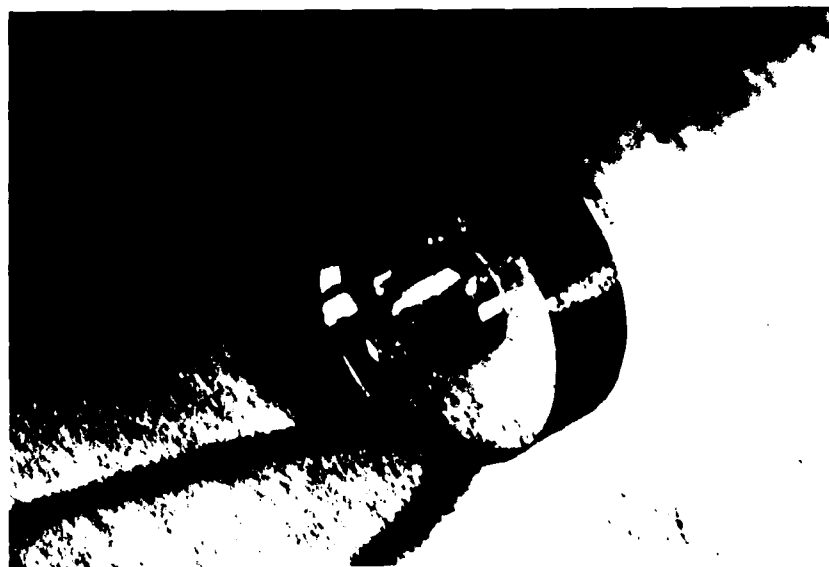


Figure 1.1 YIG Film on the Outer Surface of a GGG Ring Substrate (Sethares, 1975)

An evaluation of the thick film ring geometry was done by Poturalski in a master's thesis in 1979 (Poturalski, 1979). Large coupling variations were significantly reduced and Poturalski was able to propagate surface waves around the ring, but was unable to achieve satisfactory rotation rate sensing sensitivity. Some unexplained variations were still present.

Problem Statement and Scope

Poturalski observed a non-uniformity of coupling and dispersion as a function of lattice orientation at the

surface wave launch site (Poturalski, 1979:80). He suggested that an analysis be performed on the effect of the orientation of the crystal lattice at the surface wave launch site and the propagation direction. This suggestion serves as the premise for the present investigation.

Since the rotation rate systems proposed by Sethares use the characteristics of magnetostatic surface wave (MSSW) propagation to sense rates, the experimental analysis performed on the 1-inch YIG samples in this thesis pertains to the characteristics of surface modes only. To simplify the geometry, the orientation effects of crystalline direction were studied on flat, thin films of YIG deposited on a GGG surface.

Several characteristics of the surface mode were investigated. Insertion loss measurements between the transmitting and receiving transducers were made to observe the effects of signal power. Time delays of pulsed RF signals were included because of the MSSW's technological importance to variable time delay devices. All characteristics were measured as a function of a rotation angle (θ) which is measured relative to the crystal lattice orientation. In addition to varying the rotation angle, the receiver transducer was varied in both axes of the YIG film plane as shown in Figures 1.2 and 3.3 in order to obtain profile measurements of the wave as it travelled across the film. The ability to independently vary these parameters is

facilitated by the coupling probes designed and developed by Poturalski for the rotating YIG ring (Poturalski, 1979:39) (see Figure 3.2).

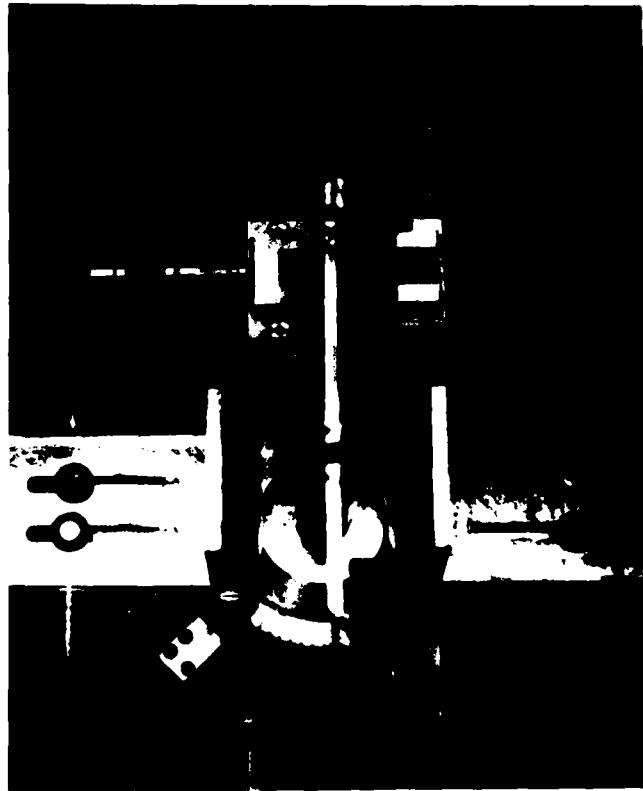


Figure 1.2 Top View of Apparatus Used in the Investigation

Although the Poturalski probes were indispensable to the rotation measurements, they were suspect for the introduction of measurement errors. An evaluation of the probes detected a steering effect. The metal cover, which was used to prevent electromagnetic radiation feedthrough, was thought to be the cause of this phenomena. An experiment to confirm the influence of a metallization spaced closely to the propagation path was performed. These measurements produced the most rewarding findings of this report.

Overview

For the reader who is unfamiliar with MSSW technology, the derivation of the electromagnetic field equations for the magnetostatic modes and surface wave propagation is discussed in the second chapter. This will enable the reader to understand the interactions of externally applied magnetic fields and ferromagnetic materials. Also, a pertinent discussion of crystallography and its importance to the investigation is included.

The design and development of experimental equipment and procedures is described in the third chapter. This chapter discusses the ferromagnetic samples, the probes used for transducers, the experimental test fixture, and two test configurations used for gathering magnetostatic characteristics versus various surface wave launch angles.

Analysis of the results obtained from the experiments are discussed in the fourth and fifth chapters. Analysis of radio frequency (RF) pulse measurements revealed a slight dependence of these magnetostatic characteristics on the surface wave launch angle. A second, more sensitive technique using an oscillating circuit, was found to verify the influence of magnetocrystalline anisotropy on the magnetostatic surface wave. A calculated shift in frequency of the oscillator was found to be in agreement with previous calculations and measurements of anisotropic constants.

It was found during the initial experiments that the probes had an influence on the pulse and oscillator

measurements. In the fifth chapter, an investigation of a metallization spaced closely to the propagation path was performed to determine its influence on the magnetostatic wave. This metallization altered the velocity of the magnetostatic wave and demonstrated, for the first time, the refraction of a magnetostatic wave.

The refraction technique may prove useful for instantaneous frequency selection in electronic counter-measure equipment. This, and other recommendations for further study, along with concluding remarks, are found in the last chapter.

II. Magnetostatic Surface Wave Theory

Background

A description of the interactions between internal magnetic moments and externally applied magnetic fields will best explain the magnetostatic behavior in ferromagnetic materials, such as yttrium-iron-garnet (YIG).

Sparks classically explains magnetostatic behavior in terms of magnetic moments due to electron spins within a crystal lattice (Sparks, 1964:5). In ferromagnetic materials, neighboring spins and their associated magnetic moments tend to be aligned parallel to one another. By integrating over a volume of these magnetic moments, one obtains a total magnetic moment which can be perturbed by external fields.

Next, considering the spin system when a DC field is applied, a change is evident. Intuitively, this field has an effect on an isolated one-spin system, and thus, on the total magnetic moment. Further, one can show how this spin system is related to the magnetic moment. A torque is produced in the presence of the DC field which causes a precession of the magnetic moment around its unperturbed position. The rate of this precession is referred to as the Larmor frequency, and the magnetic moment rotates at some precession angle that is measured with respect to the unperturbed magnetic moment direction (Figure 2.1).

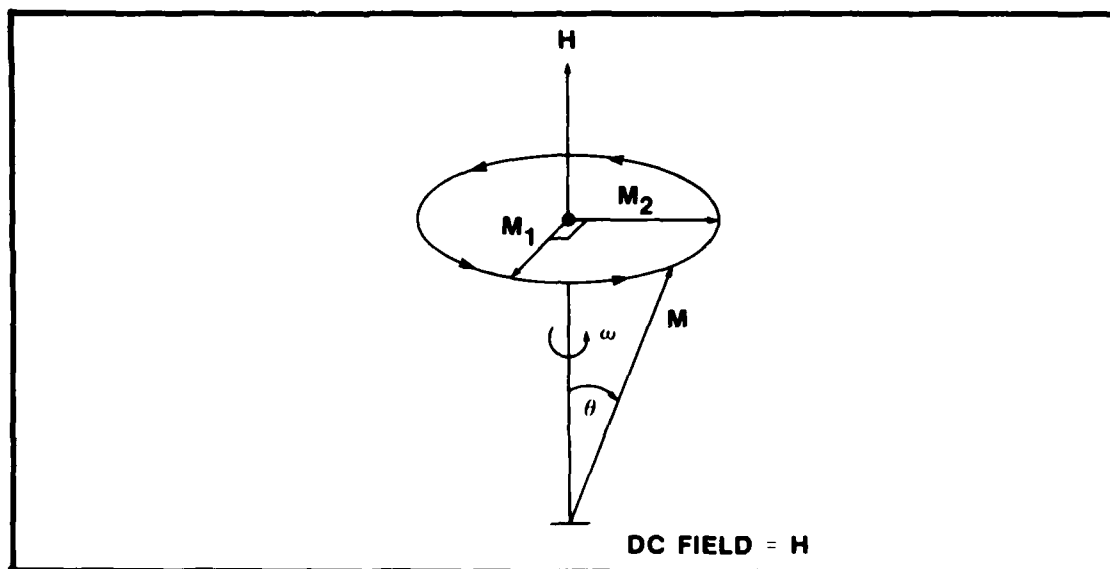


Figure 2.1 One Spin System (Sparks, 1964)

Sparks discusses the magnetic moment's reaction to an RF field applied orthogonally to the DC field. When the frequency of the RF field is set to the precessional rate of the spin system, a two-fold change is seen in the magnetic moment vector. The magnitude of the magnetic moment vector and the precession angle are both increased (Sparks, 1964:6). These changes are represented by M_1 and M_2 in Figure 2.1.

For any rotating body, the rate of change of the angular momentum \vec{J} equals the applied torque \vec{T} :

$$\frac{d\vec{J}}{dt} = \vec{T} \quad (1)$$

The precession of rotation is at a rate sufficient to conserve the initial angular momentum. Another relationship of the applied torque involves the magnetic moment:

$$\vec{m} = \gamma \vec{J} \quad (2)$$

where γ is the gyromagnetic ratio.

The torque resulting from subjecting a magnetic moment m to a magnetic field \vec{H} is given by:

$$\vec{T} = \vec{m} \times \vec{H}. \quad (3)$$

Combining (1) and (3) with (2) yields

$$\frac{d\vec{m}}{dt} = \gamma (\vec{m} \times \vec{H}) \quad (4)$$

which is the equation of motion for the magnetization (Emptage, 1982:266).

It is noted that a demagnetization appears when this single system is expanded to include more spins. This opposition is caused by a reactionary field which acts to demagnetize the applied DC field. Two properties which linearly relate to this demagnetization, \vec{H}_d , are a demagnetization factor, N_d , which is a function of the material's geometry and the saturation magnetization, $4\pi M_s$, of the ferromagnetic material (Soohoo, 1960:55).

$$\vec{H}_d = 4\pi \vec{M}_s N_d. \quad (5)$$

This alters the net effective field which now becomes

$$\vec{H}_e = \vec{H}_a - \vec{H}_d \quad (6)$$

where \vec{H}_a = applied field.

The preceding discussion does not include all physical phenomena that will affect magnetostatic behavior. Limitations in the model include omission of temperature effects, impurities, and surface defects. These issues are important and several will be discussed later, but despite these effects, the equations provide a fundamental basis for discussion of the magnetostatic surface wave mode of propagation.

Magnetostatic Surface Waves

Now, with a basic understanding of the internal magnetic characteristics of a ferrite such as YIG, we can place boundary conditions on the ferrite and introduce a current transducer which provides an external magnetic field signal we would like to propagate.

This phenomena is best analyzed by simultaneously solving Maxwell's equations and the gyromagnetic equation, along with the appropriate electromagnetic boundary conditions. Figure 2.2 illustrates the position of the boundaries. The conductor between Regions I and II represents the transducer. Region III is the YIG film. Regions I, II, and IV are air surrounding the film.

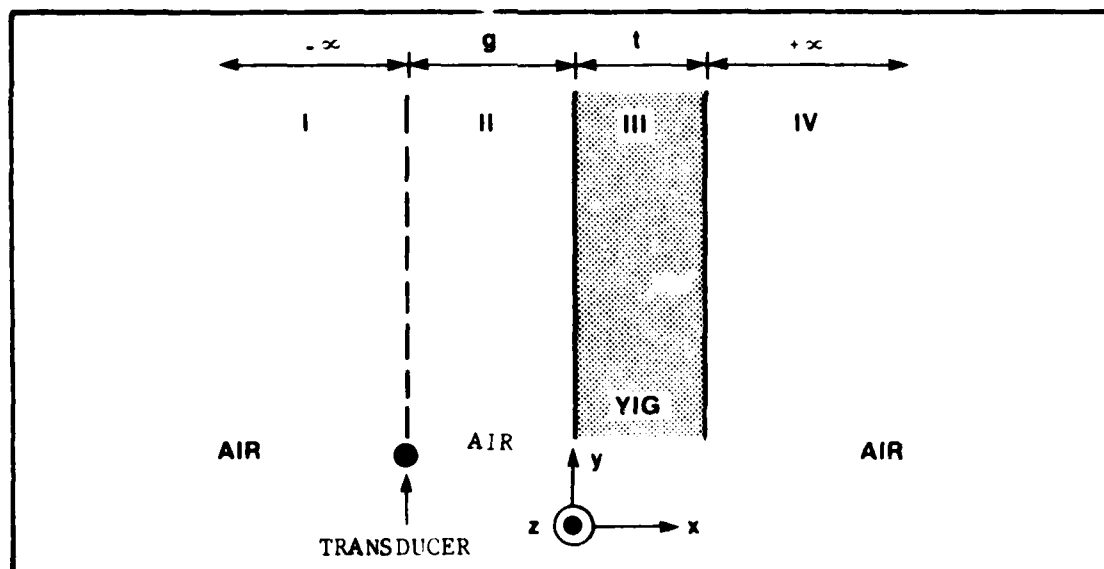


Figure 2.2 Geometry of the MSSW System

Maxwell's equations are satisfied in each of the four regions:

$$\nabla \times \vec{H} = \frac{\partial \vec{D}}{\partial t} \quad (1)$$

$$\nabla \times \vec{E} = -\frac{\partial \vec{B}}{\partial t} \quad (2)$$

$$\nabla \cdot \vec{B} = 0 \quad (3)$$

$$\nabla \cdot \vec{D} = 0 \quad (4)$$

$$\vec{B} = \mu_0 \vec{\mu}_r \cdot \vec{H} \quad (5)$$

$$\vec{D} = \epsilon \vec{\epsilon}_r \cdot \vec{E} \quad (6)$$

For MSSW propagation in the y direction,

$$H_z = E_x = E_y = 0 \quad (13)$$

and using the magnetostatic approximation (Morgenthaler, 1983:135), we assume the time rate of change of \vec{D} is approximately zero such that,

$$\frac{\partial \vec{D}}{\partial t} = \omega \epsilon E_z \approx 0 \quad (14)$$

Maxwell's equations for our magnetostatic system are now:

$$\frac{\partial H_y}{\partial x} - \frac{\partial H_x}{\partial y} = 0 \quad (15)$$

$$\frac{\partial E_z}{\partial y} = -i\omega B_x, \quad \frac{\partial E_z}{\partial x} = i\omega B_y \quad (16)$$

and

$$\frac{\partial B_x}{\partial x} + \frac{\partial B_y}{\partial y} = 0 \quad (17)$$

The next step is to satisfy the magnetization motion equation; a linear form is considered, such that

$$\vec{B} = \mu_0 \vec{\mu}_r \cdot \vec{H} \quad (18)$$

For Region III, the film's anisotropy requires

$$\vec{\mu}_r = \begin{bmatrix} \mu_{11} & i\mu_{12} \\ -i\mu_{21} & \mu_{22} \end{bmatrix} \quad (19)$$

whereas for Regions I, II, and IV, we have the unit matrix.

Using Emptage's notation (Emptage, 1982: 5122), the relative permeabilities are:

$$\mu_{11} = \mu_{22} = 1 - \Omega_H (\Omega^2 - \Omega_H^2)^{-1} \quad (20)$$

$$\mu_{12} = \Omega (\Omega^2 - \Omega_H^2)^{-1} \quad (21)$$

with

$$\Omega = \omega / 4\pi m_s \gamma \quad (22)$$

$$\Omega_H = H_e / 4\pi m_s \quad (23)$$

Now, since $D_x = D_y = 0$, and there is no z dependence of D , Equation (10) is satisfied, and it is noted that:

$$\vec{D} = \epsilon_0 \vec{\epsilon}_r \cdot \vec{E} \quad (24)$$

so

$$D_z = \epsilon_0 \epsilon_r E_z \quad (25)$$

with $\epsilon_r = 1$ for Region I, II, and IV; and $\epsilon_r = 13.0$ (Lax, 1962:703) for Region III.

Under the magnetostatic approximation, the H field may be defined in terms of a magnetic potential function where

$$\vec{H} = \nabla \Psi \quad (26)$$

In order to solve equations (15-18) with such a potential, we assume a solution of the form

$$\psi_j = (A_j e^{a_j x} + B_j e^{-a_j x}) e^{-iky} e^{i\omega t} \quad (27)$$

with $j = I, II, III, IV$ denoting the region of interest. It will be shown that a_j is positive and is determined by equations (15-18). The constants A_j and B_j are determined by the boundary conditions.

By assuming a time-invariant solution of equation (27), the variable t can be suppressed. Then, by inserting the assumed solution into equation (26), we get

$$H_{xj} = a_j (A_j e^{a_j x} - B_j e^{-a_j x}) e^{-iky} \quad (28)$$

$$H_{yj} = -ik (A_j e^{a_j x} + B_j e^{-a_j x}) e^{-iky} \quad (29)$$

in all regions with $j = I, II, III, IV$ for equations (28) and (29). From equation (18)

$$\begin{aligned} B_{xj} &= \mu_0 H_{xj} \\ B_{yj} &= \mu_0 H_{yj} \end{aligned} \quad j = I, II, IV \quad (30)$$

and for the YIG region,

$$\begin{aligned} B_{xIII} &= \mu_0 \mu_{11} a_{III} (A_{III} e^{a_{III} x} - B_{III} e^{-a_{III} x}) e^{-iky} \\ &\quad + \mu_0 \mu_{12} k (A_{III} e^{a_{III} x} + B_{III} e^{-a_{III} x}) e^{-iky} \end{aligned} \quad (31)$$

$$B_{yIII} = -\mu_0 \mu_{12} i a_{III} (A_{III} e^{a_{III} x} - B_{III} e^{-a_{III} x}) e^{-iky} \\ - \mu_0 \mu_{22} i k (A_{III} e^{a_{III} x} + B_{III} e^{-a_{III} x}) e^{-iky} \quad (32)$$

In order to determine a_j , we look for solutions to equation (17). From equation (30) we can get the following for the non-YIG regions,

$$\frac{\partial B_{xj}}{\partial x} = \mu_0 a_j^2 (A_j e^{a_j x} + B_j e^{-a_j x}) e^{-iky} \quad j=I, II, IV \quad (33)$$

$$\frac{\partial B_{yj}}{\partial y} = -\mu_0 k^2 (A_j e^{a_j x} + B_j e^{-a_j x}) e^{-iky} \quad j=I, II, IV \quad (34)$$

noting that if $a_j = |K|$, then equation (17) is satisfied. In Region III

$$\frac{\partial B_{xIII}}{\partial x} = \mu_0 \mu_{11} a_{III}^2 (A_{III} e^{a_{III} x} + B_{III} e^{-a_{III} x}) e^{-iky} \\ + \mu_0 \mu_{12} a_{III} k (A_{III} e^{a_{III} x} - B_{III} e^{-a_{III} x}) e^{-iky} \quad (35)$$

$$\frac{\partial B_{yIII}}{\partial y} = -\mu_0 \mu_{12} a_{III} k (A_{III} e^{a_{III} x} - B_{III} e^{-a_{III} x}) e^{-iky} \\ - \mu_0 \mu_{22} k^2 (A_{III} e^{a_{III} x} + B_{III} e^{-a_{III} x}) e^{-iky} \quad (36)$$

Now equation (17) will be satisfied for Region III if:

$$\mu_{11} a_{III}^2 = \mu_{22} K^2 \quad (37)$$

Where $\beta^2 = \mu_{22}/\mu_{11}$ so that $a_{III} = \beta K$, in order to satisfy equation (17).

Using equation (16) with the help of equation (30), we integrate and obtain,

$$\int -i\omega B_{xj} dy = E_{zj} = a_j \frac{\omega}{k} \mu_0 (A_j e^{a_j x} - B_j e^{-a_j x}) e^{-iky} \quad (38)$$

$$\int i\omega B_{yj} dx = E_{zj} = i\omega \mu_0 \frac{k}{a_j} (A_j e^{a_j x} - B_j e^{-a_j x}) e^{-iky} \quad (39)$$

Again, note everything is satisfied if $a_{III} = \beta K$, and

$$E_{z_{III}} = \omega \mu_0 \mu_{11} (A_{III} e^{a_{III} x} - B_{III} e^{-a_{III} x}) e^{-iky} + \omega \mu_0 \mu_{12} (A_{III} e^{a_{III} x} + B_{III} e^{-a_{III} x}) e^{-iky} \quad (40)$$

$$E_{z_{III}} = \omega \mu_0 \mu_{12} (A_{III} e^{a_{III} x} + B_{III} e^{-a_{III} x}) e^{-iky} + \omega \mu_0 \mu_{22} \frac{k}{a_{III}} (A_{III} e^{a_{III} x} - B_{III} e^{-a_{III} x}) e^{-iky} \quad (41)$$

Equations (40) and (41) are equal if equation (37) holds true. Therefore,

$$a_j = |k| \quad (42)$$

where $j = I, II, IV$, and

$$a_{III} = \frac{\mu_{22}}{\mu_{11}} |k| \quad (43)$$

Having a_j determined, we can now determine A_j and B_j via the boundary conditions.

From Figure 2.2, it can be observed the YIG sample is in free space, and there are no ground planes to consider. The conductor at $x=-g$ is where the current is introduced. The \vec{H} field will not be continuous across this boundary. The remainder of the boundary conditions are:

$$1. \quad @ x = -\infty \quad B_x = 0 \quad (44)$$

$$2. \quad @ x = -g \quad B_x \text{ is continuous} \quad (45)$$

$$3. \quad @ x = 0 \quad H_g, B_x \text{ are continuous} \quad (46)$$

$$4. \quad @ x = t \quad H, B_x \text{ are continuous} \quad (47)$$

$$5. \quad @ x = +\infty \quad B_x = 0 \quad (48)$$

From $\nabla \cdot \vec{B} = 0$, we get equation (17), and using equations (26) and (30) we obtain:

$$\mu_{11} \frac{\partial^2 \psi}{\partial x^2} + \mu_{22} \frac{\partial^2 \psi}{\partial y^2} = 0 \quad (49)$$

Thus, equation (49) reduces to the Laplacian, when $\mu_{11} = \mu_{22}$, which holds true for surface waves. This informs us that there is one, and only one, solution for ψ with the above boundary conditions imposed (Adler, 1960:521). Using our assumed solution, we need to determine A_j and B_j . In order for our solution to satisfy all K , we integrate (29) and (30) over K .

$$H_{y_j} = \int_{-\infty}^{\infty} -ik (A_j e^{ikx} + B_j e^{-ikx}) e^{-iky} dk \quad j=I, II, IV \quad (50)$$

$$H_{y_{III}} = \int_{-\infty}^{\infty} -ik (A_{III} e^{\beta|k|x} + B_{III} e^{-\beta|k|x}) e^{-iky} dk \quad (51)$$

$$B_{x_j} = \int_{-\infty}^{\infty} \mu_0 |k| (A_j e^{ikx} - B_j e^{-ikx}) e^{-iky} dk \quad j=I, II, IV \quad (52)$$

$$B_{x_{III}} = \int_{-\infty}^{\infty} \mu_0 \mu_{22} |k| (A_{III} e^{\beta|k|x} - B_{III} e^{-\beta|k|x}) e^{-iky} \\ + \mu_0 \mu_{12} K (A_{III} e^{\beta|k|x} + B_{III} e^{-\beta|k|x}) e^{-iky} dk \quad (53)$$

By writing,

$$\alpha_1 \equiv \mu_{22}\beta + s\mu_{12} \quad (54)$$

$$\alpha_2 \equiv \mu_{22}\beta - s\mu_{12} \quad ; \quad s \equiv \vec{k}/|\vec{k}| \quad (55)$$

we can write equation (53) as:

$$B_{xIII} = \int_{-\infty}^{\infty} \mu_0 |\vec{k}| (\alpha_1 A_{III} e^{\beta |\vec{k}| x} - \alpha_2 B_{III} e^{-\beta |\vec{k}| x}) e^{-i\vec{k}y} d\vec{k} \quad (56)$$

We can now apply boundary conditions at $x = -\infty$, where we can see that $B_{xj} = 0$, therefore, in Region I,

$$B_I = 0 \quad (57)$$

and at $x = -g$, $B_{xI} = B_{xII}$, and

$$A_I e^{-|\vec{k}|g} - B_I e^{|\vec{k}|g} = A_{II} e^{-|\vec{k}|g} - B_{II} e^{|\vec{k}|g} \quad (58)$$

at $x = 0$, $B_{xII} = B_{xIII}$, $H_{yII} = H_{yIII}$, so

$$A_{II} - B_{II} = \alpha_1 A_{III} - \alpha_2 B_{III} \quad (59)$$

$$A_{II} + B_{II} = A_{III} + B_{III} \quad (60)$$

at $x = t$, $B_{xII} = B_{xIV}$, $H_{yIII} = H_{yIV}$, so

$$\alpha_1 A_{III} e^{\beta |\vec{k}| t} - \alpha_2 B_{III} e^{-\beta |\vec{k}| t} = A_{IV} e^{|\vec{k}| t} - B_{IV} e^{-|\vec{k}| t} \quad (61)$$

$$A_{III} e^{\beta |\vec{k}| t} + B_{III} e^{-\beta |\vec{k}| t} = A_{IV} e^{|\vec{k}| t} + B_{IV} e^{-|\vec{k}| t} \quad (62)$$

at $x = -\infty$, $B_{xIV} = 0$, and

$$A_{IV} = 0 \quad (63)$$

From equations (57) and (58)

$$A_I = A_{II} - B_{II} e^{2ikl} \quad (64)$$

$$B_I = 0 \quad (65)$$

From equations (61), (62), and (63)

$$A_{IV} = 0 \quad (66)$$

$$B_{IV} = A_{III} e^{(1+\beta)ikl} + B_{III} e^{(1-\beta)ikl} \quad (67)$$

From equations (59) and (60)

$$A_{II} = \frac{1}{2} [A_{III} (1 + \alpha_1) + B_{III} (1 - \alpha_2)] \quad (68)$$

$$B_{II} = \frac{1}{2} [A_{III} (1 - \alpha_1) + B_{III} (1 + \alpha_2)] \quad (69)$$

Letting

$$W \equiv \left(\frac{\alpha_1 + 1}{\alpha_2 - 1} \right) \quad (70)$$

we can write equation (61) using equations (66) and (67), as

$$B_{III} = W A_{III} e^{2\beta ikl} \quad (71)$$

Next, by defining

$$X \equiv (1 + \alpha_1) e^{-\beta ikl} + (1 - \alpha_2) W e^{\beta ikl} \quad (72)$$

$$Y \equiv (1 - \alpha_1) e^{-\beta ikl} + (1 + \alpha_2) W e^{\beta ikl} \quad (73)$$

equations (68) and (69) become

$$A_{II} = \frac{1}{2} A_{III} X e^{\beta ikl} \quad (74)$$

$$B_{II} = \frac{1}{2} A_{III} Y e^{\beta |k| t} . \quad (75)$$

Using equation (65) the results can be expressed as

$$A_I = \frac{A_{III}}{2} e^{\beta |k| t} (X - Y e^{2|k|g}) \quad (76)$$

$$B_I = 0 . \quad (77)$$

Now all constraints are defined in terms of A_{III} .

One more boundary condition is needed to solve for A_{III} .

This last condition introduces the current $x = g$. That is,

$$H_{yI} - H_{yII} = J(y) . \quad (78)$$

The $J(y)$ term is a prescribed surface current distribution function. In order to account for the generation of all possibilities, equation (78) is written as an integral over K . That is,

$$H_{yJ} = -i \int_{-\infty}^{\infty} K (A_J(K) e^{iKx} + B_J(K) e^{-iKx}) e^{-iky} dk \quad J=I, II \quad (79)$$

at $x = g$, and

$$J(y) = -i \int_{-\infty}^{\infty} K (A_I(K) e^{iKg} + B_I(K) e^{-iKg} - A_{II}(K) e^{iKg} - B_{II}(K) e^{-iKg}) e^{-iky} dk . \quad (80)$$

Multiplying both sides by $e^{ik'y}$ and integrating with respect to y from $-\infty$ to ∞ , the result is

$$i \int_{-\infty}^{\infty} J(y) e^{-ik'y} dy = \int_{-\infty}^{\infty} \int_{-\infty}^{\infty} k \left[(A_I(k) - A_{II}(k)) e^{ik'g} + (B_I(k) - B_{II}(k)) e^{-ik'g} e^{i(k'-k)y} \right] dy dk \quad (81)$$

By noting the following two definitions, the Fourier transform of $J(y)$ is:

$$\int_{-\infty}^{\infty} J(y) e^{-ik'y} dy = \mathcal{J}(k') \quad (82)$$

and with the Dirac delta function:

$$\int_{-\infty}^{\infty} e^{i(k'-k)y} dy = 2\pi \delta(k'-k) \quad (83)$$

equation (81) reduces to

$$i \mathcal{J}(k') = \int_{-\infty}^{\infty} k \left[(A_I(k) - A_{II}(k)) e^{ik'g} + (B_I(k) - B_{II}(k)) e^{-ik'g} \right] \delta(k'-k) dk \quad (84)$$

Upon evaluation, the result is

$$\frac{i \mathcal{J}(k)}{2\pi} = k \left[(A_I(k) - A_{II}(k)) e^{ik'g} + (B_I(k) - B_{II}(k)) e^{-ik'g} \right] \quad (85)$$

by the sifting property of the delta function (Marsden, 1981:392).

Using the constraints found from the boundary conditions, equation (85) reduces to

$$\frac{i \mathcal{J}(\kappa)}{2\pi} = \kappa \left[\left(\frac{A_{\text{III}}}{2} e^{\beta \kappa t} (X - Y e^{2i\kappa g}) - \frac{A_{\text{III}}}{2} X e^{\beta i \kappa t} \right) e^{i\kappa g} + \left(-\frac{A_{\text{III}}}{2} Y e^{\beta i \kappa t} \right) e^{-i\kappa g} \right] \quad (86)$$

and upon simplification, becomes

$$\frac{i}{2\pi} \mathcal{J}(\kappa) = \frac{A_{\text{III}}}{2} \kappa e^{\beta i \kappa t} \left[((X - Y e^{2i\kappa g}) - X) e^{i\kappa g} - Y e^{-i\kappa g} \right] \quad (87)$$

Therefore, with

$$Z \equiv [((X - Y e^{2i\kappa g}) - X) e^{i\kappa g} - Y e^{-i\kappa g}] \quad (88)$$

then

$$A_{\text{III}} = \frac{i \mathcal{J}(\kappa)}{\pi \kappa e^{\beta i \kappa t}} \cdot \frac{1}{Z} \quad (89)$$

Using substitution and equation (74)

$$A_{\text{II}} = \frac{i \mathcal{J}(\kappa)}{2\pi \kappa} \cdot \frac{X}{Z} \quad (90)$$

and from equations (75), (76), and (77)

$$B_{\text{II}} = \frac{i \mathcal{J}(\kappa)}{2\pi \kappa} \cdot \frac{Y}{Z} \quad (91)$$

$$A_{\text{I}} = \frac{i \mathcal{J}(\kappa)}{2\pi \kappa} \cdot \frac{(X - Y e^{2i\kappa g})}{Z} \quad (92)$$

$$B_I = 0 \quad (93)$$

Using equation (71), and upon simplification

$$B_{III} = W \frac{i \mathcal{J}(k)}{\pi k} \cdot \frac{e^{\beta |k| t}}{Z} \quad (94)$$

From equations (65) and (67), these constraints can now be defined as

$$A_{IV} = 0 \quad (95)$$

$$B_{IV} = (1 + W) \frac{i \mathcal{J}(k)}{\pi k} \cdot \frac{e^{|k| t}}{Z} \quad (96)$$

From equations (50)-(53), the field equations can be expressed in terms of the current density. They are:

$$H_{yI} = \frac{1}{2\pi} \int_{-\infty}^{\infty} \mathcal{J}(k) \frac{(X - Y e^{2|k|g}) e^{|k|x} e^{-iky}}{Z} dk \quad (97)$$

$$H_{yII} = \frac{1}{2\pi} \int_{-\infty}^{\infty} \mathcal{J}(k) \frac{(X e^{|k|x} + Y e^{-|k|x}) e^{-iky}}{Z} dk \quad (98)$$

$$H_{yIII} = \frac{1}{2\pi} \int_{-\infty}^{\infty} \mathcal{J}(k) \frac{(e^{\beta |k|x} + W e^{2\beta |k|t} e^{-\beta |k|x}) e^{-iky}}{Z} dk \quad (99)$$

$$H_{yIV} = \frac{1}{2\pi} \int_{-\infty}^{\infty} \mathcal{J}(k) \frac{(1 + W) e^{|k|t} e^{-|k|x} e^{-iky}}{Z} dk \quad (100)$$

$$B_{xI} = \int_{-\infty}^{\infty} \frac{i\mu_0}{2\pi} \frac{|k|}{k} \frac{\mathcal{J}(k) (X - Y e^{2|k|g}) e^{|k|x} e^{-iky}}{Z} dk \quad (101)$$

$$B_{xII} = \int_{-\infty}^{\infty} \frac{i\mu_0}{2\pi} \frac{|k|}{k} \frac{\mathcal{J}(k) (X e^{|k|x} - Y e^{-|k|x}) e^{-iky}}{Z} dk \quad (102)$$

$$B_{x_{III}} = \int_{-\infty}^{\infty} \frac{i\mu_0\mu_{22}}{2\pi} \frac{|k|}{k} \frac{\mathcal{J}(k)(1 - We^{2\beta|k|t})}{Z} e^{-iky} + \frac{i\mu_0\mu_{11}}{2\pi} \frac{|k|}{k} \frac{\mathcal{J}(k)(1 + We^{2\beta|k|t})}{Z} e^{-iky} dk \quad (103)$$

$$B_{x_{IV}} = \int_{-\infty}^{\infty} \frac{-i\mu_0}{\pi} \frac{|k|}{k} \frac{\mathcal{J}(k)(1+W)e^{ik|t|}e^{-ik|x|}e^{-iky}}{Z} dk \quad (104)$$

where:

$$W = (\alpha_1 + 1) / (\alpha_2 - 1) \quad (105)$$

$$X = (1 + \alpha_1)e^{-\beta|k|t} + (1 - \alpha_2)e^{\beta|k|t} \quad (106)$$

$$Y = (1 - \alpha_1)e^{-\beta|k|t} + (1 + \alpha_2)e^{\beta|k|t} \quad (107)$$

$$Z = [((X - Ye^{2|k|g}) - X)e^{ik|g|} - Ye^{-ik|g|}] \quad (108)$$

Thus, all of the constants have been solved for in terms of the current density. The integral field equations summarized in equations (97)-(104) have been evaluated by the method of residues (Sethares, 1978:14). These equations are consistent with those of Sethares (Sethares, 1978), and may be used as a starting point for calculating the power flow for MSSW's, which may be useful in future investigations.

From Figure 2.2, it is observed that the magnetostatic wave propagates in the y-direction with an amplitude dependence on x (Sethares, 1975:13). The DC magnetic biasing field is in the z-direction.

Since the wave is guided along the surface perpendicular to the magnetic biasing field, it is given the name surface wave. Experiments by Brundle and Freedman verify the direction of propagation and conclude that a surface wave is indeed present (Brundle, 1968:1090).

Another characteristic of a MSSW is that it is dispersive. This means that the velocity of the wave is a function of frequency. This relationship is useful for interpreting some of the results from the time delay measurements, and it is shown in the following equation and Figure 2.3 (Sethares, 1975:14) that:

$$\left(\frac{\omega}{\gamma}\right)^2 = H_e^2 + 4\pi M_s H_e + \frac{1}{4} (4\pi M_s)^2 (1 - e^{-2kt}) \quad (109)$$

where k = MSSW wave number

t = thickness of YIG

ω = MSSW angular frequency

$\gamma = 2\pi (2.8 \times 10^6) \text{ Hz/Oe}$ = gyromagnetic ratio.

Crystallography

In his thesis, Poturalski (Poturalski, 1979:81), recommended the investigation of crystalline structure effects on MSSW propagation. What follows is a brief description of basic crystallography and, specifically, the crystalline structure of yttrium-iron-garnet, which is a popular propagation media for MSSW. This analysis provides information on how the orientation angle influences the magnetostatic wave.

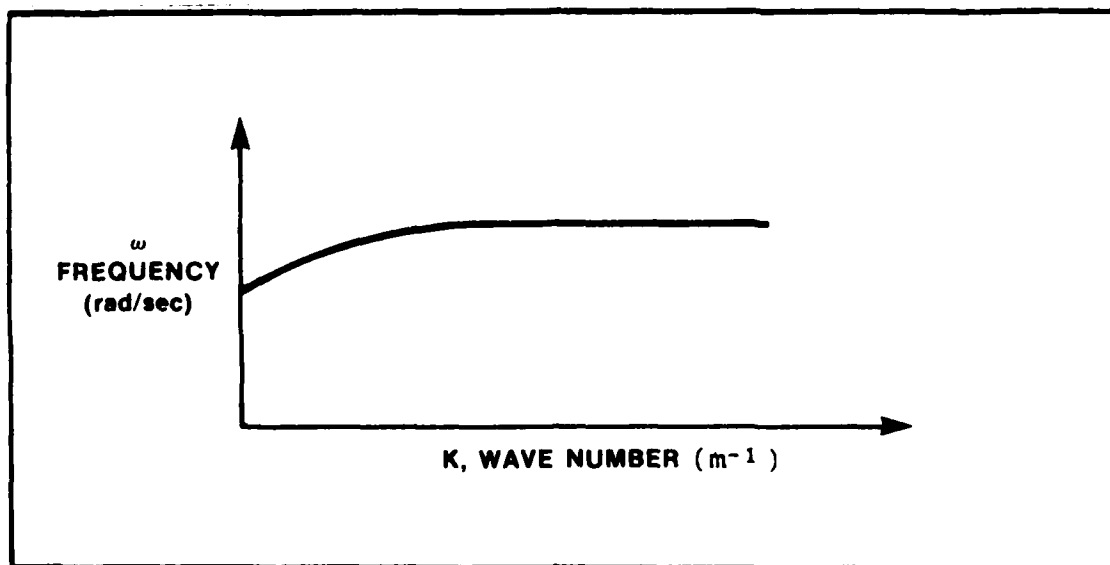


Figure 2-3 Dispersion Relation for MSSW (Sethares, 1975:18)

The various planes that pass through a crystal may be described in terms of the reciprocal of the intercepts of that plane with the crystallographic axes. These are written as $(h\ k\ l)$, with h, k, l usually expressed as the smallest possible set of integers having the same ratio. This notation format is known as the Miller index (Wood, 1963:8). A bar over an index number denotes a negative intercept.

When one refers to a particular crystalline direction, the format is to enclose the Miller index in brackets. For example, the notation $[111]$ is the direction of a vector normal to the surface of a (111) plane.

It is now of interest to introduce the structure of YIG. The samples to be investigated are all thin films grown on a gadolinium-gallium-garnet substrate. The films were

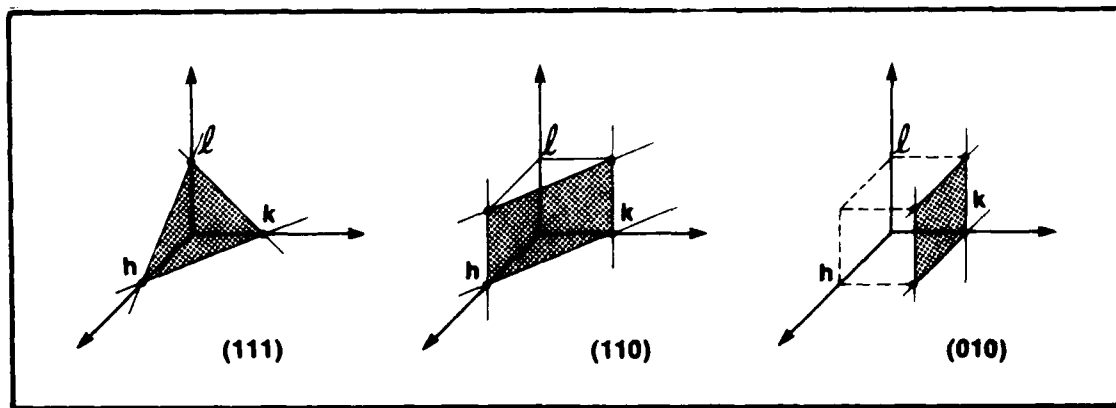


Figure 2.4 Examples of Low Index Planes (Kleber, 1970:40)

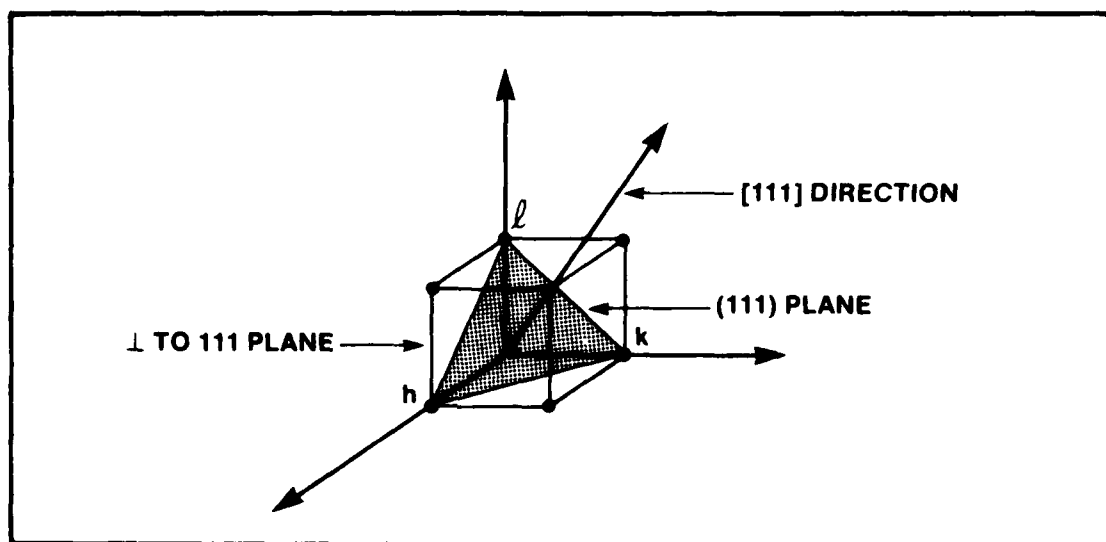


Figure 2.5 Example of Crystalline Direction (Kleber, 1970:29)

grown by liquid phase epitaxy; thus, the YIG will take the same single crystal structure as the GGG. All samples tested had (111) surfaces ([111] direction is normal to the surface of the sample).

By looking at this structure from a top-down view, as in Figure 2.6, one can see that the lattice structure exhibits three high symmetry directions.

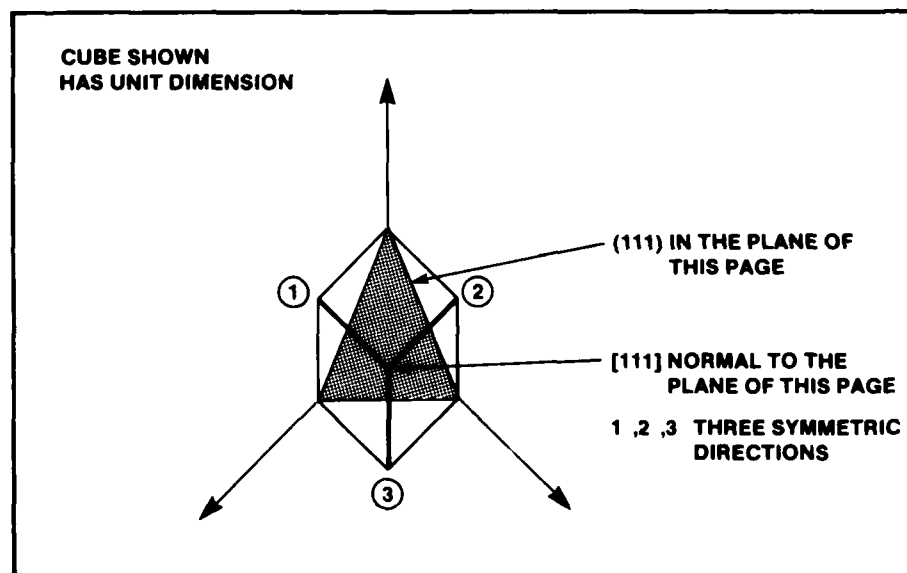


Figure 2.6 Top View of YIG Single Crystal

These three primary lattice directions are indicative of the major crystalline anisotropic variations expected for the magnetostatic surface wave. Since experiments involve a 360° rotation of the sample, the threefold symmetry is expected to lead to a sixfold dependence.

To test for crystal orientation dependence, it was necessary to construct a suitable test fixture to rotate the samples. This experimental apparatus is discussed in Chapter Three, along with the test circuit configurations.

III. Experimental Apparatus and Procedures

Sample and Probes

The films used in Sethares' and Poturalski's investigations were grown on cylindrical surfaces. The waves were launched by a fine wire located close to the YIG surface. The direction of propagation is noted by the wave vector k in Figure 3.1. These investigations were unique in that no one had ever propagated MSSW's in this fashion. Conventional delay lines were generally fabricated from samples cut from films grown on 1- to 3-inch diameter GGG flat wafers.

Earlier experiments in microwave magnetics were performed with YIG rods and slabs fabricated from bulk crystals. Since large defect-free samples are difficult to realize, a more uniform process is desired. An outgrowth of the development of magnetic bubble memories was the advent of growing large homogeneous thin films of YIG. The technique used to fabricate these single crystal films is liquid phase epitaxy (LPE). A "melt" is prepared with the proper composition and heated to just above the saturation temperature of about 910 C. When the temperature of the melt is brought below saturation, crystallization occurs. A suitable substrate is brought to the same temperature before being immersed in the solution, and serves as a seed for crystallization. The growth of YIG on GGG is relatively fast--on the order of one micron per minute. The GGG has relatively the same lattice constant as YIG. Pure YIG has

a lattice constant which is about 0.06% smaller than that of GGG (Glass 1982:102). A defect-free substrate generally leads to good epitaxial growth. Substitutions may be made in the melt to help compensate for the lattice mismatch, but these impurities also alter the magnetic properties of the film. Therefore, substitution is used as a trade-off which allows growth of thick films for certain device applications, or to provide temperature compensation of the material for other applications (Glass, 1982:104). For example, it has been found that when the lead content of the melt equals the platinum impurity concentration, the melt produces films which have the narrowest FMR (Ferro-Magnetic Resonance) line-width (a measurement of loss quality) and smallest lattice misfit (Glass, 1976:288).

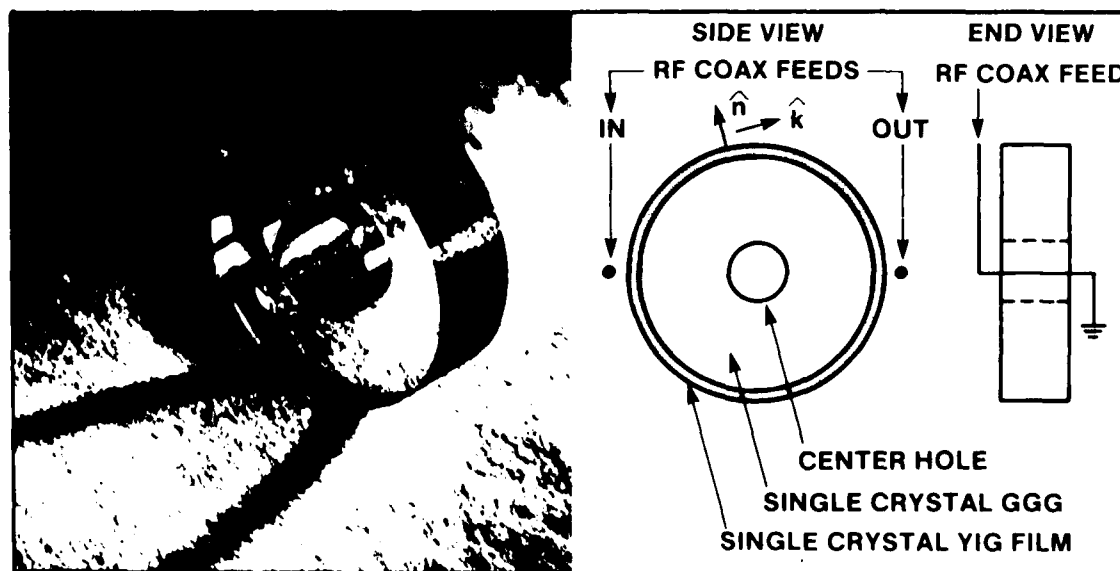


Figure 3.1 Diagram of YIG Film Used for Rotation Rate Sensing

Upon review of the fabrication process of YIG films, several reasons for anisotropic characteristics are evident. One prospect is uniformity. If the film thickness is not uniform, it has been shown that magnetic properties will vary. Another reason for anisotropy is the stress induced by the lattice mismatch. Lattice mismatch is the main cause of material defects. There is also magnetocrystalline anisotropy, which Poturalski thought to be the main cause of his poor propagation results (Poturalski, 1979:79). He felt that the cubic structure beneath the launch transducer had an effect on the coupling efficiency.

For normal delay line configurations, the relative position of the transducer and the film does not change: but with the rotation rate sensor, the change relative to the transducer is three-dimensional. This investigation will use Poturalski's launch transducers on a flat sample, with rotation in the plane of the single crystal film, and thus, its cubic structure will be available for investigation (Figure 3.2). The Poturalski transducers were chosen for two reasons. One, they provide an ability to launch magnetic waves with adjustable coupling, and second, they provide high isolation because of their RF shielding properties.

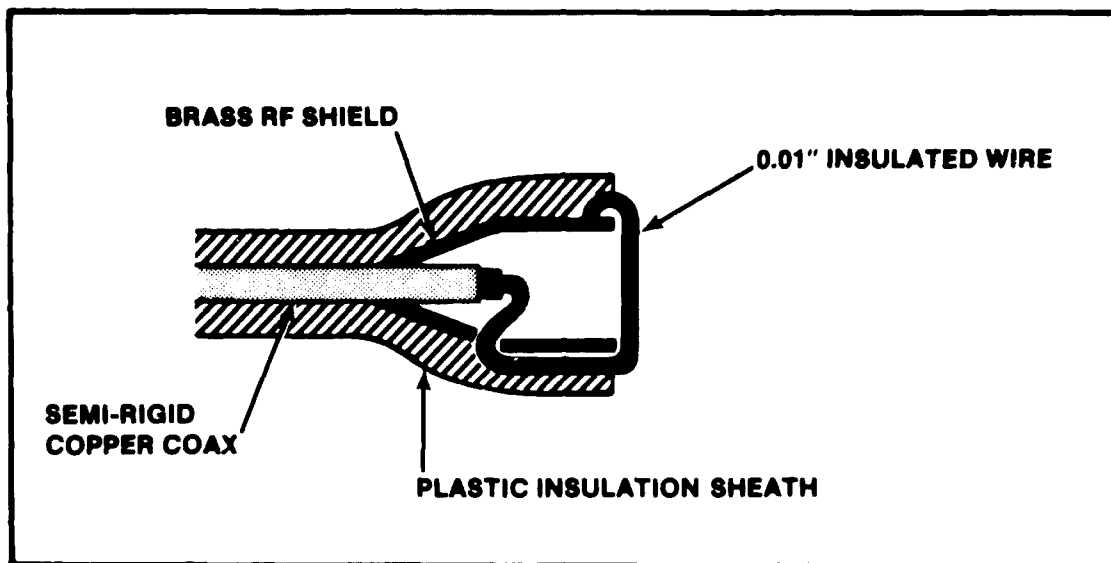


Figure 3.2 Cross-Section View of Poturalski Probe
(Poturalski, 1979:42)

The experiments detected and recorded the influence of the crystallographic structure on the propagation characteristics of magnetostatic waves. These probes were a key factor in the evaluation of the microwave properties that were under investigation. They permitted the fabrication of a simple delay line in the magnetostatic surface wave configuration, a simple single wire transducer to launch the wave, and another for the detection of the surface wave.

Normal evaluation of a delay line involves several characteristics, two of which include insertion loss and time delay. These characteristics will be measured and recorded as a function of the rotation angle θ (Figure 3.3).

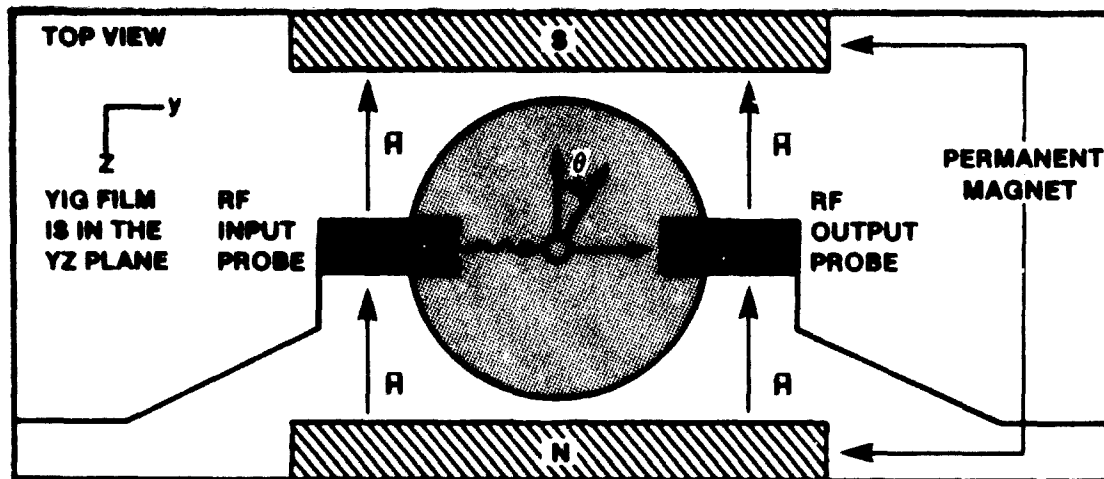


Figure 3.3 Orientation of Disc to Rotation Angle θ . (Top View) (After Poturalski, 1979:78)

As noted in the previous chapter, the films under investigation had (111) surfaces. Any influence of the crystallographic structure should have three high-symmetry directions, as the sample is rotated from 0° to 360° . There should be a sixfold dependency present, and its influence is what this investigation is trying to analyze.

The samples to be tested were provided by James Sethares of the Rome Air Development Center, Hanscom AFB, MA. The three samples were grown by the LPE method. The film thicknesses were 11.5, 7.35, and 7.5 microns for the three samples. Each had a small lead impurity, which tended to help the tensile misfit; thus, the samples should have very little stress induced anisotropy (Glass, 1982:102).

Experimental Setup

A test apparatus was designed for accurate placement and measurement of input and output probes. By noting the basic test configuration shown in Figure 3.3, it can be observed that the design of the apparatus had to permit both rotation of the disc for the basic anisotropic data, and accurate movement of the transducers to collect beam steering data when anisotropic effects influenced the direction of propagation. The testing apparatus is pictured in Figure 3.4.



Figure 3.4 Test Apparatus

The Poturalski probes were attached to micrometer adjustable translation stages. The input probe varied only in the x-direction in order to optimize RF coupling and facilitate the insertion and removal of samples. The output probe was mounted on a three-dimensional stage. In this way, beam steering could be investigated, as well as time delay and amplitude distributions. The 1-inch diameter YIG films with 500 μm GGG were mounted on a $\frac{1}{4}$ -inch (6.35mm) plexiglass

disc, and then mounted onto the 2-inch high stand. The stand was circular, with angles marked between 0° and 360° , in 5° increments. The machining of the stand was accomplished to an accuracy of ± 1 degree of arc. Three-inch square permanent magnets were mounted on adjustable slides in order to provide variable magnetic bias fields. The permanent magnets provided a field strength ranging from 0 to 800 Gauss.

Pulse Measurements

The circuit depicted in Figure 3.5 was developed for testing the RF characteristics. A continuous wave (CW) sinusoidal signal generator was gated with a PIN diode switch. The gated RF signal was split by a 10dB coupler, and the main signal was passed through a tuner, for matching purposes, and then to the MSSW delay line and a TWT amplifier before detection. The coupled signal was used as a reference.

From this configuration, data was obtained in three categories, which include signal power, time delay, and beam steering of the magnetostatic delay pulse. The YIG samples were rotated through 360° , with data being taken at 10 increments. Since the single wire transducers produce a wideband signal, the frequency used for testing was adjusted to minimize insertion loss when the magnetic bias field (H) was fixed at 300 Gauss. Evaluation of the results of these investigations are reported in Chapter Four.

What one observes from the resulting data of the gated RF measurements is some very erratic, if not random, data. These findings led to testing the apparatus, with the delay line in place, on a network analyzer. This procedure permitted a frequency domain picture of the device to be taken. Observation of the delay line's passband shifting up and down in frequency, when the film was rotated beneath the transducers, led to testing the device in an oscillator configuration.

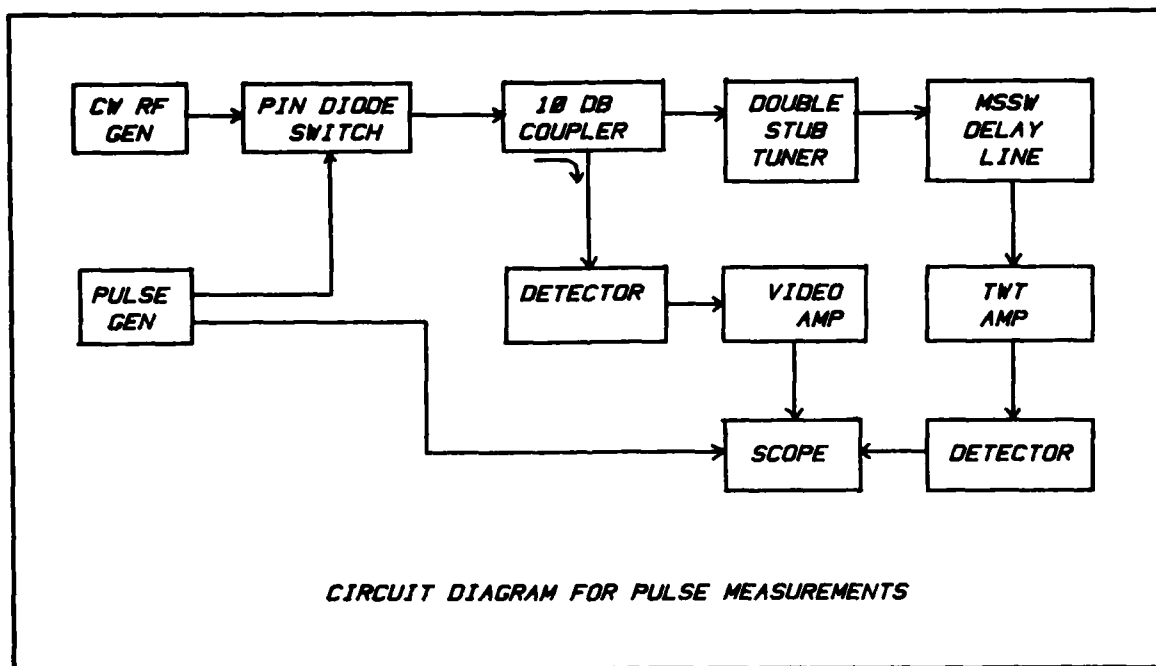


Figure 3.5 Block Diagram for RF Pulse Measurements

Delay Line Oscillator

A delay line oscillator circuit was possible, since there would be no need to change the delay line configuration of the test apparatus (see Figure 3.6). In this apparatus,

all parameters were held constant, except for rotation of the YIG film. The data obtained from this testing showed a definite crystallographic influence and will be presented in the next chapter.

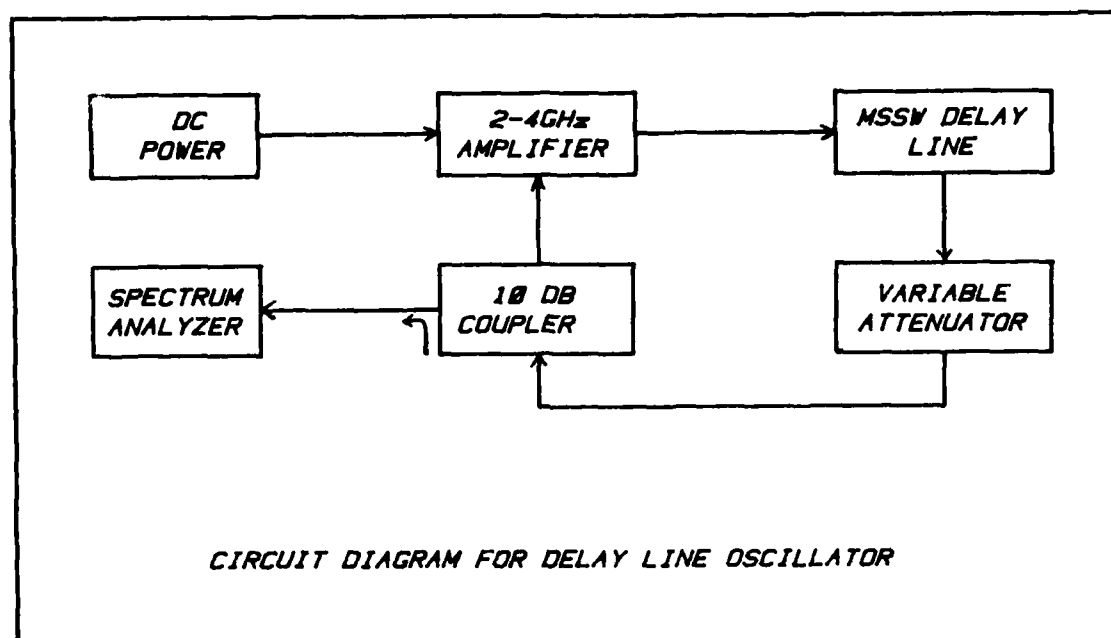


Figure 3.6 Circuit for Delay Line Oscillator Test

IV. Experimental Results and Findings

Pulse Measurements

As described in Chapter Three, the test fixture was constructed to accurately hold the transmitting and receiving probes for profiling the characteristics. Most of the experiments used CW pulses at 2400 MHz (s-band). Among the first data to be taken were the field profiles.

In Figure 4.1, the three-dimensional shape of the amplitude distribution can be observed. This general shape was true for all the YIG samples. In Figure 4.2a, a cross-section of the amplitude distribution is shown. The data of Figure 4.2a was taken in the YZ plane with $z=10\text{mm}$. The hump shape in the exponential falloff is due to reflection from

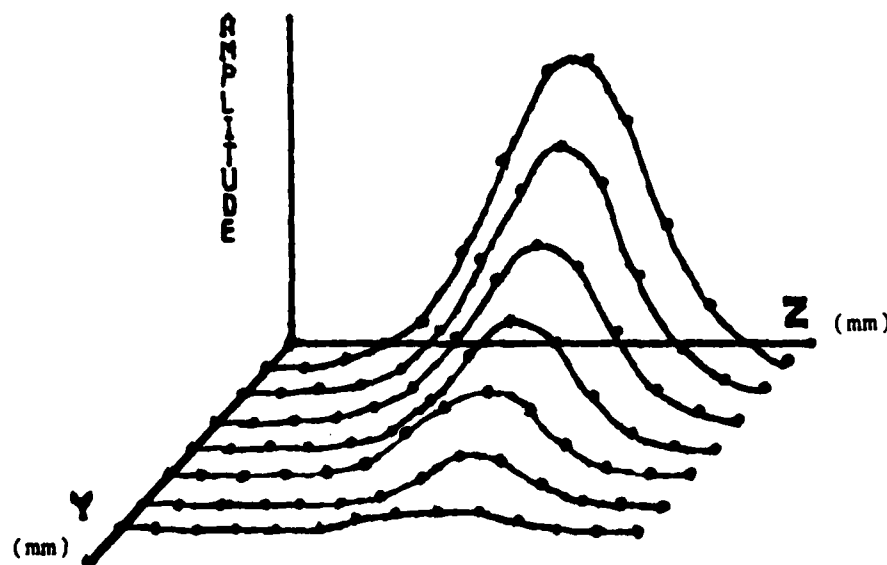


Figure 4.1 Amplitude Distribution of MSSW Beam

the sample edge. Figure 4.2b shows the time delay of a 5 nsec wide pulse through the magnetic medium as a function of path length in meters.

From Figure 4.1, it can be observed there is a slight steering of the beam to the left. This steering effect changed as the sample was rotated. At times, the beam would be steered to the right, but this did not have a sixfold dependence. Measurements of the MSSW beam in the x-y plane provide a cross-sectional view of the time delay profile or amplitude roll off. A set of measurements was also taken with $Y = \text{constant}$ for the beam steering profiles.

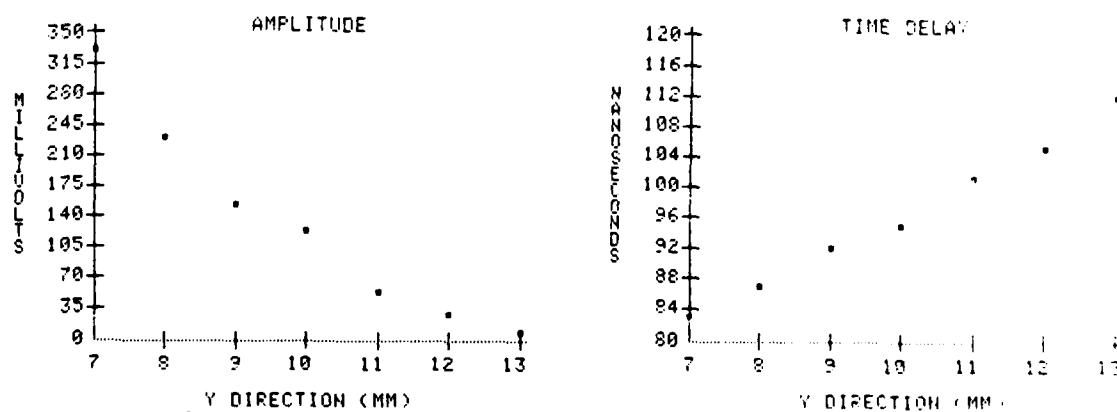


Figure 4.2.a.) Amplitude Profile b.) Time Delay Profile

The resultant data was then plotted for evaluation. Some of the resultant graphs are depicted in Figures 4.3 and 4.4. Data was taken at 10° increments and normalized to the greatest value to emphasize any periodicity. Visual inspection of the data in Figures 4.3 and 4.4 shows some random nature, and it is very difficult to deduce anything directly. However, techniques do exist for evaluation of the apparently random data. A correlation analysis was helpful in interpreting these results.

The autocorrelation function will be examined first. The use of this technique will emphasize any major periodicities which may be present in the data. The autocorrelation function, $R(\theta)$, in discrete form is:

$$R_X(\theta) = \frac{1}{N-\theta} \sum_{n=1}^{N-\theta} X_n X_{n+\theta} \quad \theta = 0^\circ, 10^\circ, 20^\circ \dots 350^\circ \quad (110)$$

In order to validate the technique, a random number generator was used to create test data with a sixfold dependency added in. The data is pictured in Figure 4.5 with its autocorrelation. The correlation function was able to identify the sixfold periodicity. There is, however, a drawback to autocorrelation. This technique may tend to hide one periodicity if a more dominate periodicity is present. Therefore, a technique called cross-correlation is sometimes used. This function is similar to autocorrelation, but instead of correlating data with itself, it is correlated with a known function containing the dependence one is

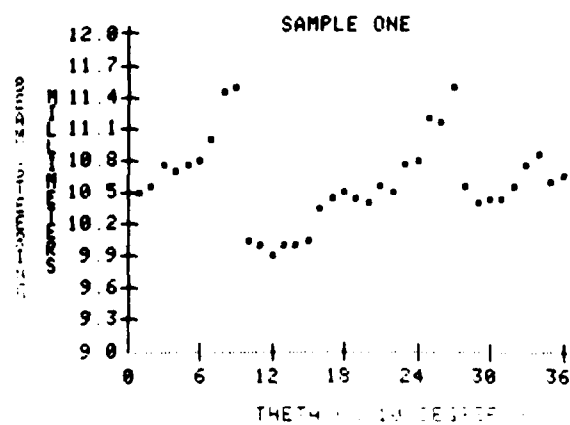
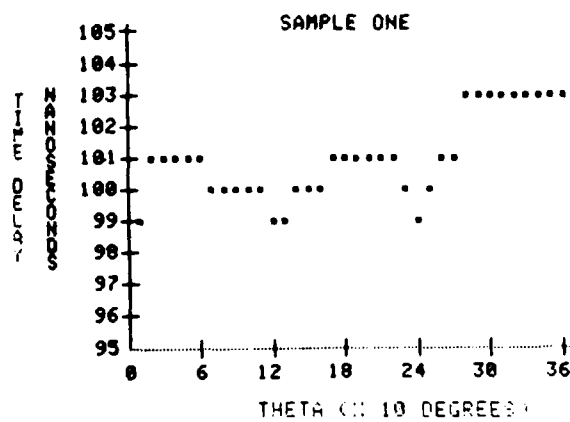
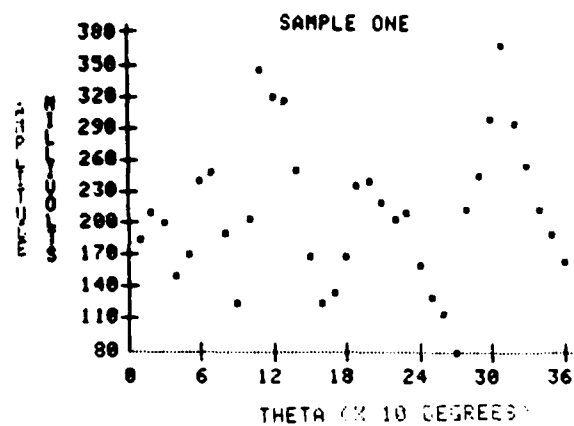


Figure 4.3 Sample One, Pulse Measurements of
a) amplitude, b) time delay, and c) beam steering

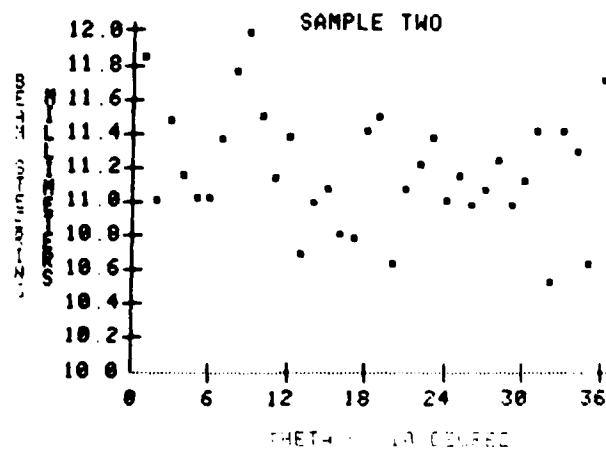
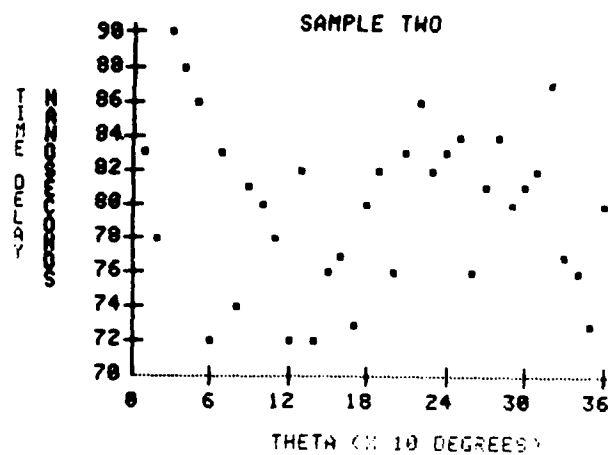
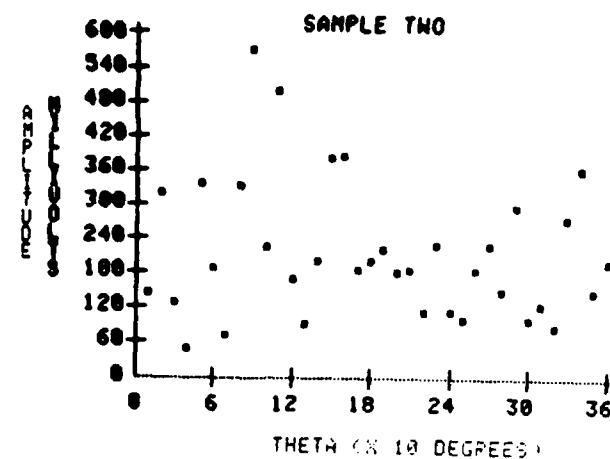


Figure 4.4 Sample Two, Pulse Measurements of
a) amplitude, b) time delay, and c) beam steering

searching for. Thus, comparison of cross-correlations will reveal the relative strengths of the periodicity.

One of the main reasons for using correlation techniques is evident from the data in Figure 4.4. The amplitude data seems to have no evident periodicity, but when the autocorrelation is evaluated, one can see a noticeable twofold dependency present in Figure 4.6c. There is also some evidence of a sixfold dependency. In Figure 4.6, several correlation graphs are presented for the experiments performed on signal strengths and time delays. These graphs show the general trend of this data. They are not very convincing, however, because the sixfold crystal symmetry has such a large effect on the magnetostatic wave.

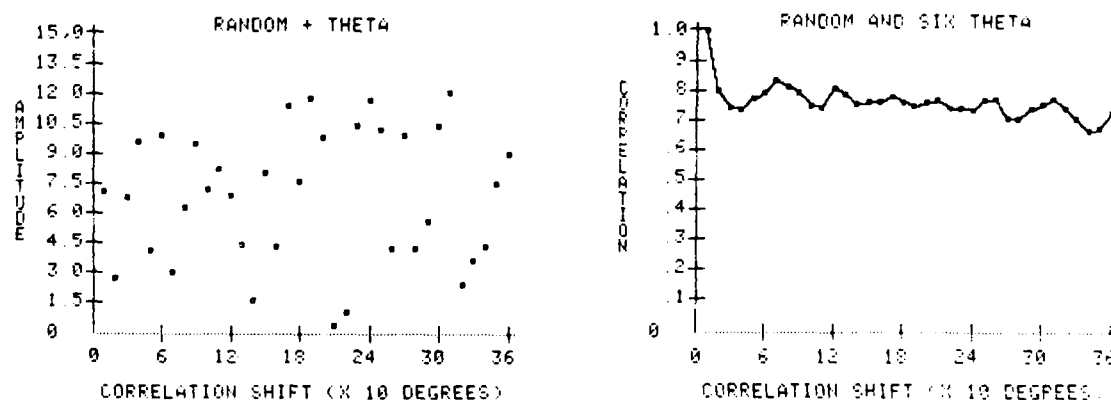


Figure 4.5 a) Random Test Data with Sixfold Dependence Added
b) Autocorrelation

The facts or conclusions which could be drawn from these first experiments were unconvincing for a sixfold dependence. Other characteristics were sought and investigated to find if, indeed, there was any sixfold influence.

Figure 4.7 shows actual data correlation graphs of insertion loss, group delay, and group velocity. These results were also not at all conclusive. However, when this data was taken, the group delay data was derived from the phase measurement on a network analyzer. The network analyzer, which could display amplitude and phase of the transmission characteristic versus frequency, revealed some interesting results. The amplitude versus frequency response illustrated the bandpass or "passband" of the delay line. When the YIG sample of the delay line was rotated, one could see the passband shifting up and down in frequency. This shifting appeared to be related to the internal DC field bias, because holding θ constant and varying the DC bias caused the same result. This observation motivated oscillator experiments which looked for frequency shifts related to the crystalline anisotropy.

Delay Line Oscillator Measurements

The circuit for frequency shift effects must be able to detect small frequency variations in the samples. One way to achieve this is to test the sample as a resonator. The optimum and easiest way, however, is to use it as an oscillator. By using the YIG sample as a delay line in the feedback loop of a delay line oscillator, the frequency of oscillation becomes sample dependent. A diagram of the circuit is shown in Figure 4.8.

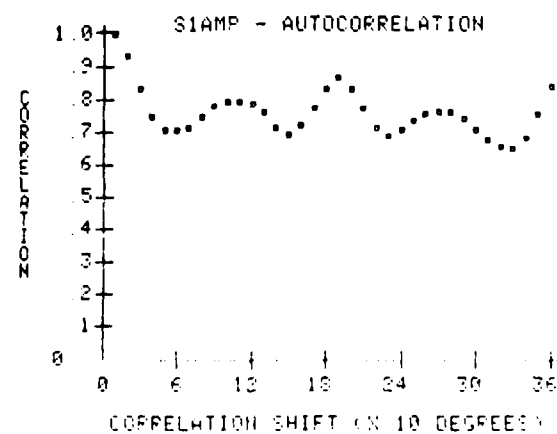
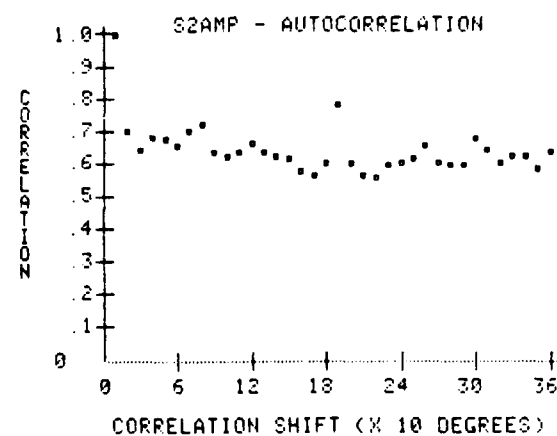
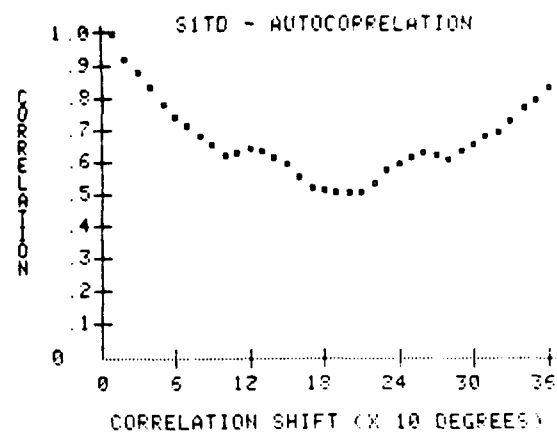


Figure 4.6 a) Sample One, Time Delay Autocorrelation
 b) Sample Two, Amplitude Autocorrelation
 c) Sample One, Amplitude Autocorrelation

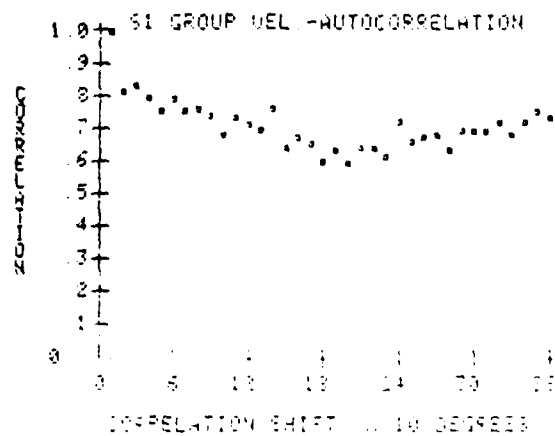
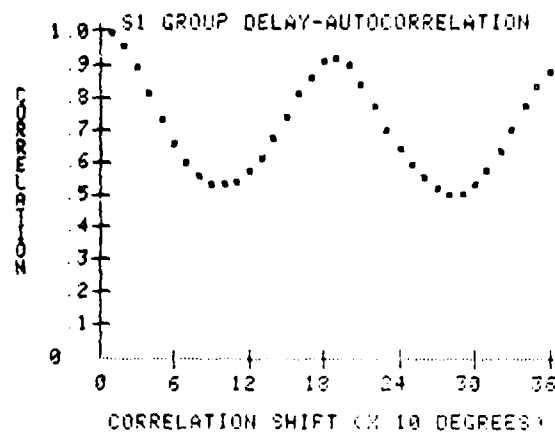
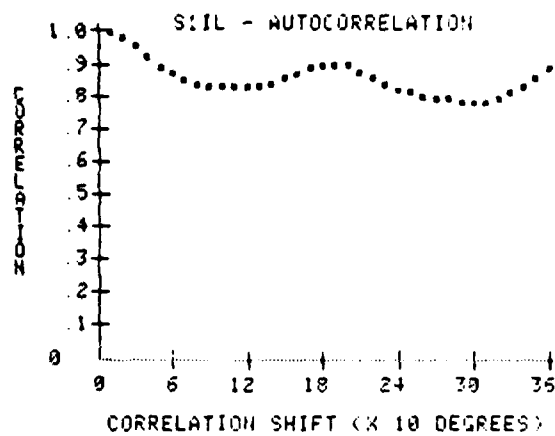


Figure 4.7 Correlation graphs of
 a) IL-Insertion Loss
 b) GD-Group Delay
 c) GV-Group Velocity

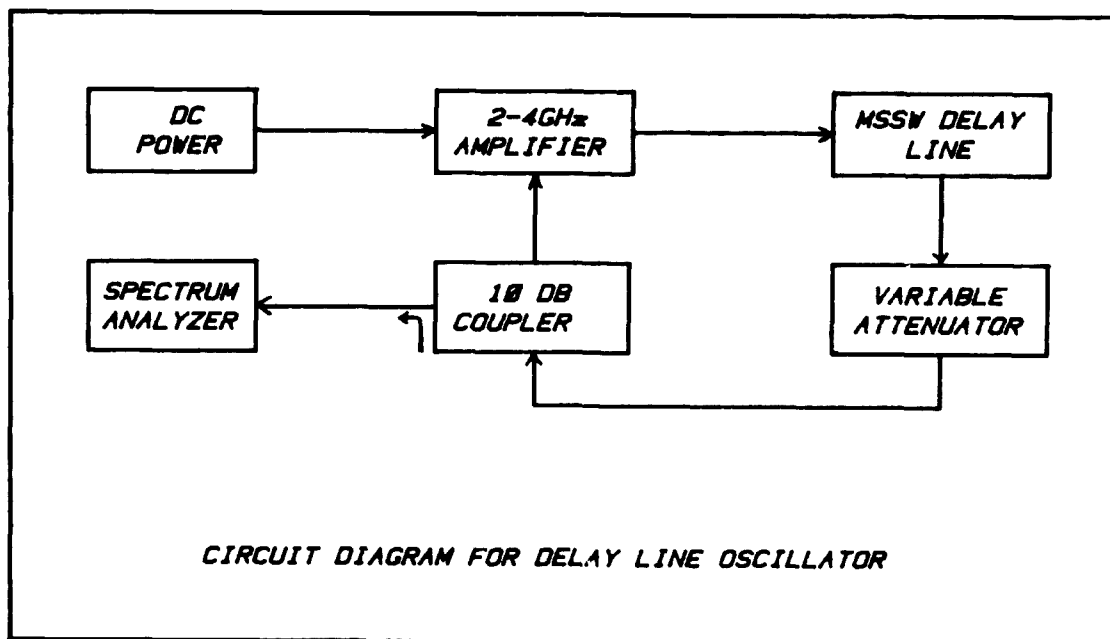


Figure 4.8 Block Diagram of the Delay Line Oscillator

When these tests were performed, everything was held constant, except the rotation angle (θ). The gain of the loop was adjusted such that only one frequency was oscillating. It was easy to track a particular wave number in this way. As the net effective field in the YIG was altered due to the rotating sample, the frequency of oscillation shifts slightly. In this way, measurements were taken for F versus θ , and the results are displayed in Figure 4.9. The sixfold dependency is easily identifiable, even on top of a twofold dependency. The sixfold dependence is more noticeable in the second sample as compared to the first sample. The maximum frequency shift occurred, however, in the first sample and it was 24.35 MHz (peak to valley).

The autocorrelations of Figure 4.10 show the definite sixfold dependency. The cross-correlations of Figure 4.11 allow comparison of the sixfold dependency between samples. It should be noted here that the amount of sixfold dependency found in each sample is inversely related to the thickness of the sample, but it is not proportional. Recall that sample thicknesses were 11.5, 7.35, and 7.5 microns for samples one, two, and three, respectively. Although this is interesting, no solid conclusion can be drawn from it.

There was another factor which also influenced the testing, and it was investigated further. From Figure 4.1, the three-dimensional plot of the amplitude, it can be seen that the maximum amplitude occurred slightly off the center line of the sample. It was found that when everything was held constant, including the rotation angle (θ), the location of the maximum amplitude signal could be changed by adjusting the CW frequency of the pulses. This beam steering phenomenon was recorded and examined in Chapter Five.

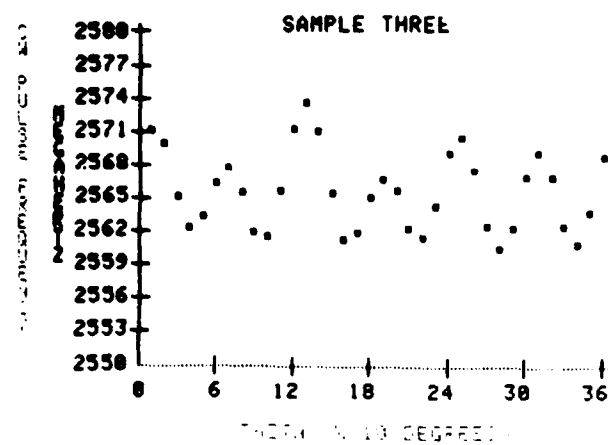
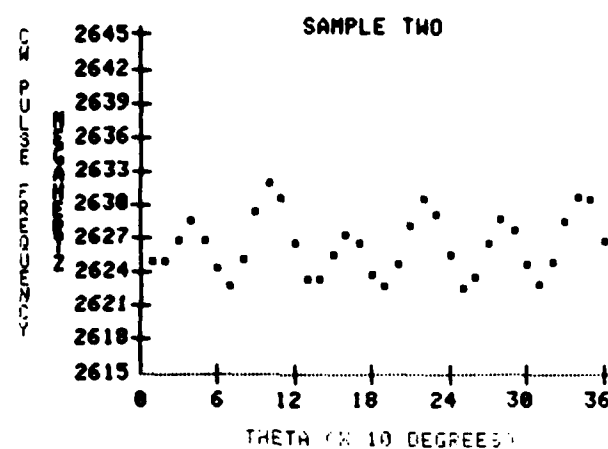
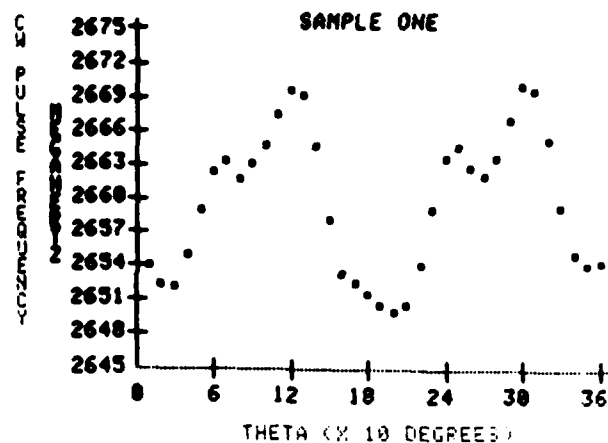


Figure 4.9 Frequency Shifts Versus Rotation Angle θ

- a) Sample One
- b) Sample Two
- c) Sample Three

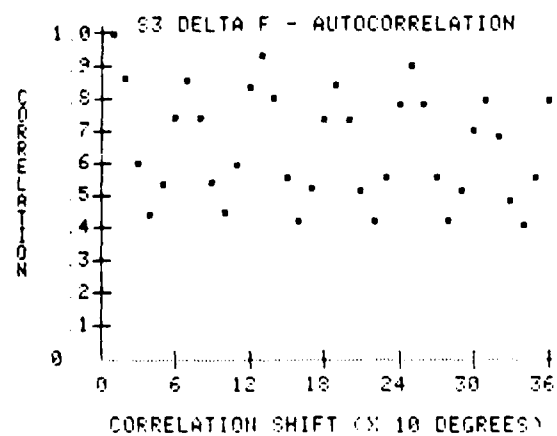
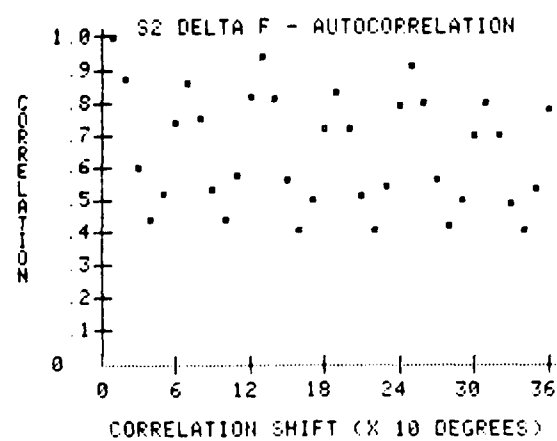
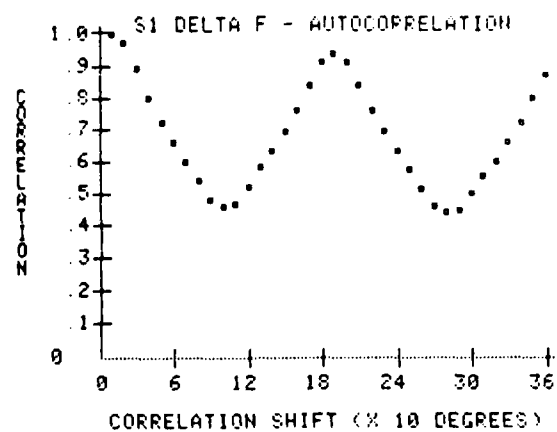


Figure 4.10 Autocorrelations for Figure 4.9 Data
 a) Sample One
 b) Sample Two
 c) Sample Three

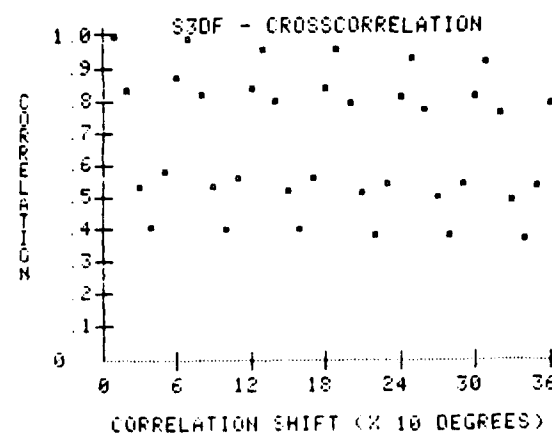
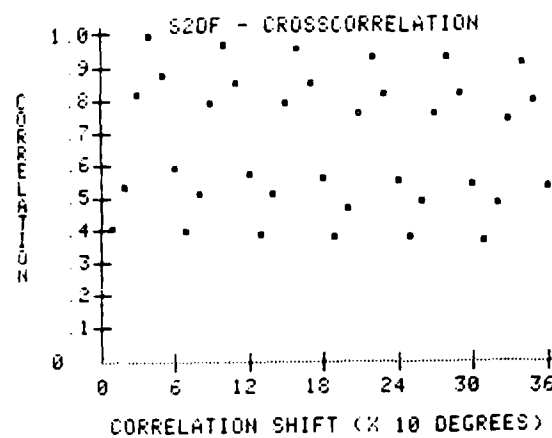
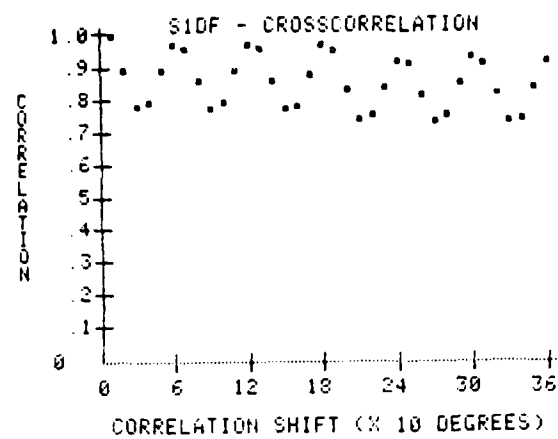


Figure 4.11 Cross Correlations of Figure 4.9 Data
 a) Sample One
 b) Sample Two
 c) Sample Three

V. Beam Steering

As mentioned in earlier chapters, there were experiments performed where the effects of beam steering were present, in addition to the crystalline anisotropy influence. It was found, for example, that with all parameters held constant, including θ , that the position of maximum signal strength (beam steering) could be altered by simply changing the CW frequency of the pulsed signals. Some data was taken, and a plot of the results is shown in Figure 5.1.

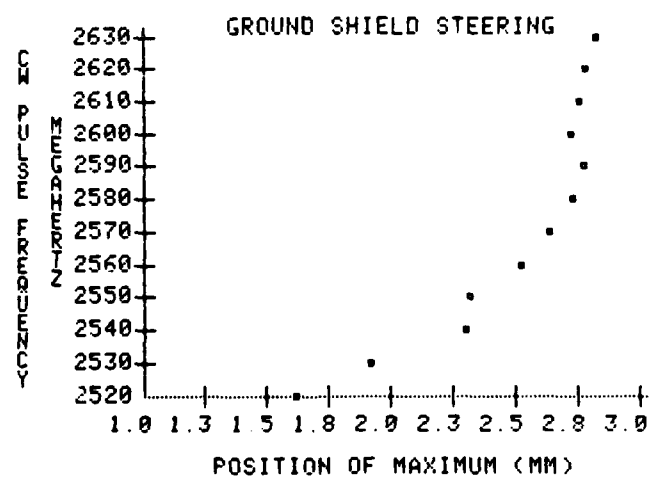


Figure 5.1 Beam Steering as a Function of Frequency

Upon examination of the test apparatus, it was found that the input probe/transducer RF shield was not parallel to either the sample or the transducer. This was suspected to be the cause of the frequency dependent steering because

conductors are known to influence magnetostatic waves, and this non-uniformity was probably causing some interference.

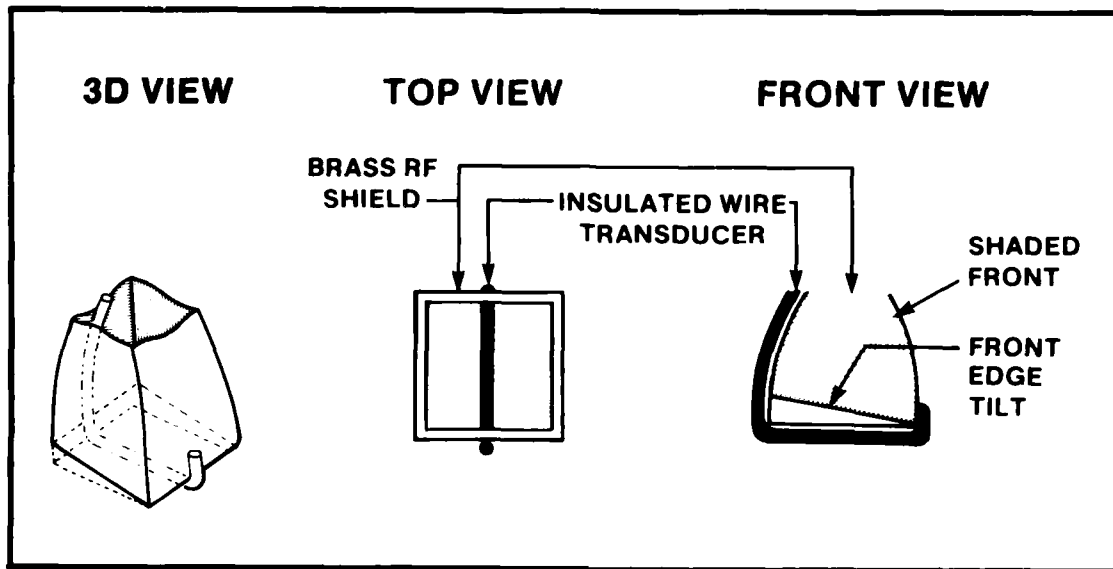


Figure 5.2 View of Non-Parallel RF Shield

To understand how this physical perturbation may affect the MSW beam, we need to view a sketch of the geometry. Figure 5.3 illustrates the regions close to the transducer. The beam passes through Region 2, which represents the non-parallel shield. The velocity in this region is a function of the spacing of the shield. Since the spacing is tilted, the velocity is a function of y . The frequency of the wave remains the same, but the velocity changes, and thus, so does the wavelength. A theoretical expression was sought to model this case, but none was satisfactorily obtained.

In order to prove the concept of conductor metallization steering, a more simplistic geometry was conceived. The basic geometry is that of an oblique incidence of a magnetostatic wave upon a metallization boundary located near the input transducer. Figure 5.4 depicts this scenario.

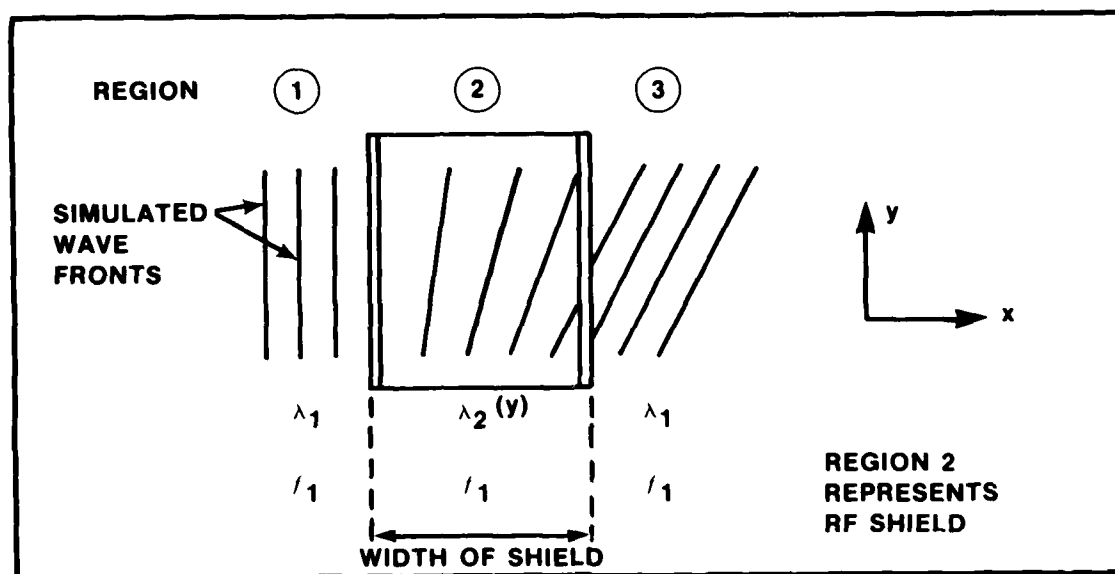


Figure 5.3 Regions of RF Shield Interface

Region 1 is the metallization area. The wave front of an MSW beam meets the boundary at an angle of 25° , assuming the beam to be of width, W . The velocity in Region 1 will be faster than Region 2 for a frequency, f_1 . If the beam meets the interface at an angle of 25° , the left edge of the beam will have to travel the distance, D_1 , in Region 1. Then, while the left edge of the beam travels, D_1 , the right edge will travel D_2 . This boundary difference in velocities causes what is commonly known as refraction.

The angle of refraction is calculated below:

$$\tan \Omega = \tan 25^\circ \left(1 - \frac{K_1}{K_2} \right) \quad (111)$$

where K_1 and K_2 are the MSSW wave numbers in their respective regions.

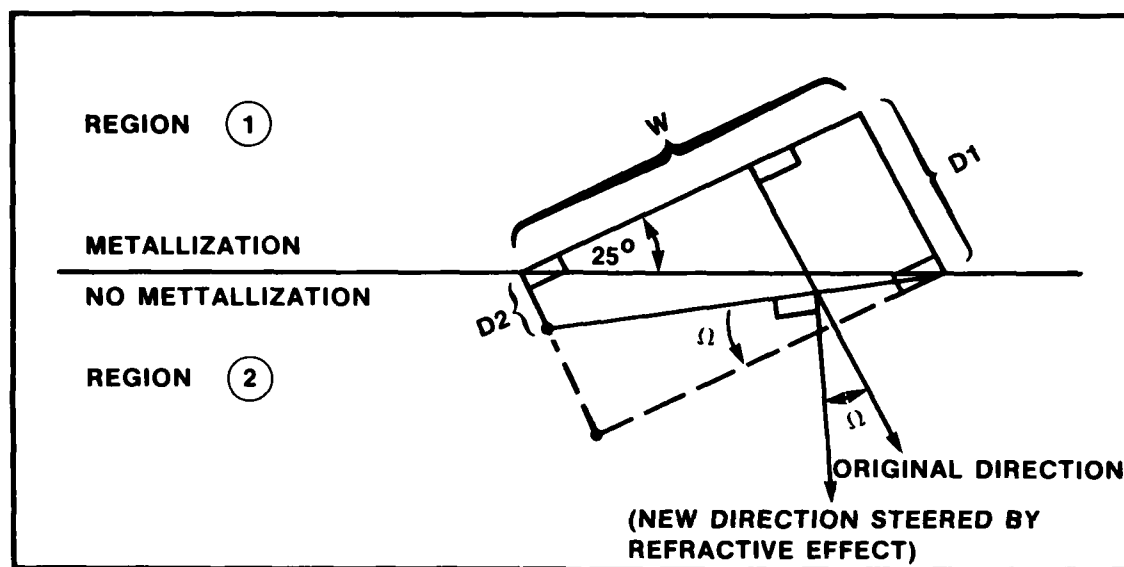


Figure 5.4 Diagram of the Oblique Incidence

A test fixture was constructed to verify this refraction steering. The device is pictured in Figure 5.5. The gold triangular metallization and transducers were deposited onto an alumina substrate. The substrate is 10 mils thick, with metallization totally covering the bottom side to provide a ground plane. The input wave initially strikes the triangle at a right angle. This boundary has a negligible effect on the shape of the wave; it primarily increases its velocity. The refraction is created at the oblique second interface. Since this fixture did not lend

itself well to probing, a semi-circle of receivers was arranged approximately 1 inch from the input. This apparatus provided for a more stable and controlled experiment.

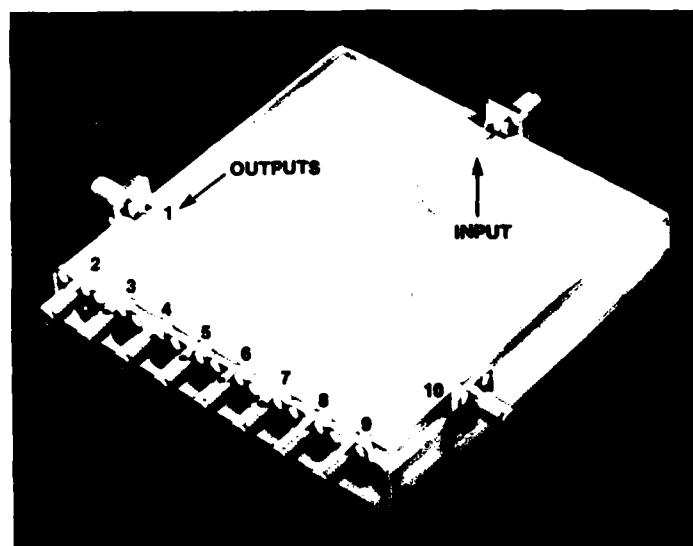


Figure 5.5 Test Apparatus for Examining Beam Steering

Since magnetostatic waves are dispersive, it is easily confirmed that it is the velocity differential across the boundary that can steer the MSW beam. The dispersive nature propagates different frequencies at different velocities; therefore, different frequencies will be steered by differing amounts. Figure 5.6 demonstrates this property. Two pulses of different CW frequencies were propagated through the triangular metallization region. While the pulse of a 3.10 GHz signal was steered to receiver number four, the pulse of a 3.55 GHz signal was received at channel three. The first demonstration of the property of refraction in magnetostatic

waves was performed with this device. Thus, it has been shown that the metallization does indeed have an affect on the magnetostatic wave. This is convincing evidence which supports the conclusion that the tilting RF shield did influence and bias the measurements of the probe apparatus.

SEPARATION OF TWO SIMULTANEOUS CW PULSES

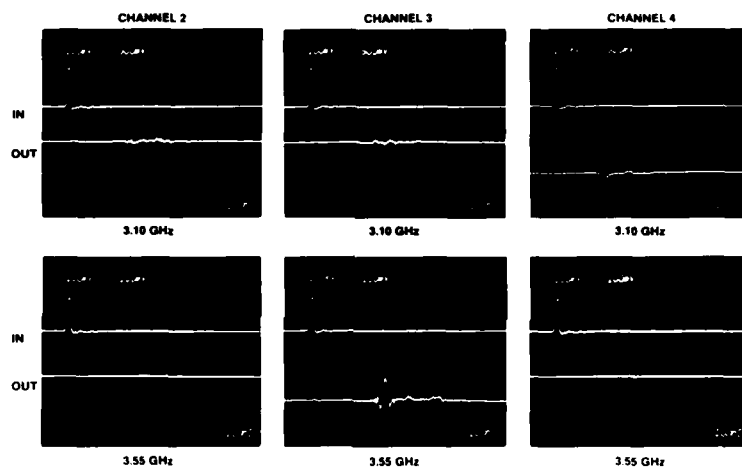


Figure 5.6 Separation of Pulse with Differing CW Frequencies

VI. Conclusions and Recommendations

This thesis investigated anisotropic effects in magnetostatic surface waves. There were several experiments performed during this investigation, and important conclusions may be drawn from them. The first experiments were simple delay line measurements of samples at variable input and output transducer locations. The samples were rotated beneath the transducers, while data for signal attenuation, time delay, and beam steering were collected. These measurements resulted in the collection of what appeared to be very random data. Auto- and cross-correlation techniques were used to analyze the data. It was found that there were indeed periodicities present in the data. A twofold periodicity, or every 180° , was observed in some of the data. This was expected, since whenever the sample was mounted at a slight tilt from the horizontal, the twofold dependency resulted from the fact that when rotated 180° , the sample would be at the same tilt angle, but propagation would be in the opposite direction. Even with random data and a dominant twofold dependency, a sixfold crystallographic dependency was detected.

The second set of experiments involved measurement of the YIG samples using a network analyzer. For a delay line configuration, insertion loss, group delay and group velocity data were recorded. All of the data was found to be

consistent with known MSW characteristics. It was from these measurements that a frequency shifting effect was noticed.

The delay line oscillator measurements revealed the most informative crystallographic results. This configuration was more sensitive to the anisotropic effects, which change the effective H field acting on the magnetic spins of the thin ferrite film. The frequency of oscillation is directly dependent on the applied and effective H field. The oscillation frequency was shifted slightly by a relative rotation between the sample and the transducers. This shift was shown to have sixfold symmetry through a rotation of 360°. The amount of shift is in close agreement with anisotropic constants of YIG measured by other methods. A theoretical shift for Δf , using these anisotropic constants, was calculated to be 19 MHz as compared to the measured results of 24 MHz shown in Chapter Four. These results represent a third technique for the measurement of the magnetocrystalline anisotropy and show agreement with the results of Sethares and Tsai (Sethares, 1977:1236), and their ferromagnetic resonance technique and Hanna, et al, for their surface acoustic wave phase shift technique (Hanna, 1983:1803). The oscillator experiment is the first positive verification of anisotropic effects on the propagation of magnetostatic surface waves.

The work, which studied the beam steering effects of the Poturalski probes, helped produce the most rewarding results. As a result of the findings, a second test fixture

was constructed to verify the amount of influence of a closely spaced metal conductor. The geometry of the fixture enabled the first demonstration of magnetostatic wave refraction.

In summary, this investigation verified the existence of anisotropic effects. It was shown that the amount of influence is negligible in delay lines. However, for applications which are highly frequency dependent, such as an oscillator or a phase shifter, there is a need to include magnetocrystalline constants. The results of this thesis agree with measured magnetocrystalline constants of Everett and Hughes (Everett, 1970:1120). The delay line oscillator results are a new way to identify and predict the influence of magnetocrystalline anisotropy on magnetostatic surface waves.

Recommendations

A recommendation for further study concerning anisotropic effects, would be to devise a more accurate scheme for mounting the sample transducers, which would make their contributions of mounting error less significant. This would, hopefully, reduce some of the random fluctuations of data taken for the delay line signal strengths, time delays, and beam steering. Another suggestion would be to use a narrowband transducer to generate fewer frequencies for propagation across the sample. This would enable the experimenter to more accurately track the signal path and its characteristics.

The work, which explored the phenomena of MSW refraction, shows promise as a frequency separator and should be investigated further. It should be possible to exploit the features of refraction for frequency selective and/or dependent devices for use in electronic warfare counter-measure applications. A U.S. patent application for such a device has been filed (Floyd, 1984).

Bibliography

1. Adler, R. B., L. J. Chu, and R. M. Fano, Electromagnetic Energy Transmission and Radiation. New York, N.Y.: John Wiley & Son, Inc., 1960.
2. Brundle, L. K. and N. J. Freedman, "Magnetostatic Surface Waves on a YIG Slab." Electronics Letters, 4:132-134 (1968).
3. Collins, J. H., J. D. Adam, and Z. M. Bardai "One-Port Magnetostatic Wave Resonator," Proceedings of the IEEE, pp. 1090-1092 (July 1977).
4. Damon, R. W. and J. R. Esbach, "Magnetostatic Modes of a Ferromagnetic Slab," J. Phys. Chem. Solids, 19:308-320 (Nos. 3/4, 1961).
5. Emptage, P. R., "Generation of Magnetostatic Surface Waves by a Microstrip," J. Appl. Phys., 53 (7):5122-5125 (July 1982).
6. Everett, G. E. and R. S. Hughes, "FMR with the Magnetic Field in a (111) Plane of a Cubic System," J. Appl. Phys., 41:1120-1121 (No. 3, 1970).
7. Floyd, R. E., U.S. Patent Application, Serial Number 627699, filed 3 July 1984, at Waltham, MA, U. S. Air Force Invention Number 16,383.
8. Glass, H. L., "Epitaxial Ferrites for Magnetostatic Wave Devices," Proceedings of the 1981 RADC Microwave Magnetic Technology Workshop, June 10-11, 1981, RADC-TR-83-15 (January 1983).
9. Glass, H. L. and M. T. Elliott. "Attainment of the Intrinsic FMR Linewidth in Yttrium Iron Garnet Films Grown by Liquid Phase Epitaxy." J. Crys. Growth, 34:285-288 (1976).
10. Hanna, S. M., F. J. Friedlaender, R. L. Gunshor, and H. Sato, "Propagation of Surface Acoustic Waves in Magnetic Bubble Garnet Films." IEEE Transactions on Magnetics, 19 (5):1802-1804 (September 1983).
11. Hayt, W. H., Jr., "Engineering Electromagnetostatic Surface Waves by a Microstrip," J. Appl. Phys., 53 (7):5122-5125 (July 1982).
12. Kleber, Will, An Introduction to Crystallography. Berlin, German Democratic Republic: VEB Verlag Technik Berlin, 1970.

13. Lax, B. and K. J. Button, Microwave Ferrites and Ferrimagnetics. New York, N.Y.: McGraw-Hill, 1962.
14. Marsden, J. and B. Tromba, Vector Calculus, Second Edition. San Francisco, CA: W. H. Freeman, 1981.
15. Miller, N. D. J. and D. Brown, "Turnable Magnetostatic Surface Wave Oscillator," Electronics Letters, 12:209-210 (1976).
16. Morgenthaler, F. R., "Field Gradient Control of Magnetostatic Waves for Microwave Signal Processing Applications," Proceedings of the 1981 RADC Microwave Magnetic Technology Workshop, June 10-11, 1981, RADC-TR-83-15 (January 1983).
17. Newburgh, R. G., P. Blacksmith, A. J. Budreau, and J. C. Sethares, "Acoustic and Magnetic Surface Wave Ring Interferometers for Rotation Rate Sensing," Proceedings of the IEEE, 62:1621-1628 (December 1974).
18. Poturalski, R. J., Rotation Rate Sensing Via Magnetostatic Surface Wave Propagation on a Thick YIG Ring, Master of Science Thesis, AFIT-GE-EE-79-28. Air Force Institute of Technology, Wright-Patterson AFB, OH (December 1979).
19. Sethares, J. C., Magnetostatic Surface Waves on a Cylinder, Air Force Cambridge Research Laboratory Technical Report, AFCRL-TR-75-0380 (July 1975).
20. Sethares, J. C. and T. Tsai, "Magnetic Anisotropy of (111) LPE-YIG Films on G³ in Parallel Resonance," IEEE Transactions on Magnetics, 13 (5):1236-1237 (September 1977).
21. Soohoo, R. F., Theory and Application of Ferrites. Prentice-Hall, Inc., New Jersey, 1960.
22. Sparks, M., Ferromagnetic-Relaxation Theory. New York, N.Y.: McGraw-Hill, 1964.
23. Wood, Elizabeth A. Crystal Orientation Manual. New York, N.Y.: Columbia University Press, 1963.

VITA

Captain Robert E. Floyd was born on the third of April 1957, in Tulsa, Oklahoma, to James L. and Faye H. Floyd. He attended Memphis Preparatory School and received his high school degree in May 1975. He graduated from the University of Mississippi and was awarded the Bachelor of Science in Electrical Engineering degree in May 1979.

Upon graduation, he received his commission in the United States Air Force through ROTC. He entered the Air Force Institute of Technology in June 1979 and is pursuing a Master of Science degree in Electrical Engineering.

Permanent Address: 1680 Timothy Dr.
Memphis, TN 38116

Unclassified

SECURITY CLASSIFICATION OF THIS PAGE

REPORT DOCUMENTATION PAGE

1a. REPORT SECURITY CLASSIFICATION Unclassified			1b. RESTRICTIVE MARKINGS <i>A172375</i>		
2a. SECURITY CLASSIFICATION AUTHORITY			3. DISTRIBUTION/AVAILABILITY OF REPORT Approved for public release; distribution unlimited.		
2b. DECLASSIFICATION/DOWNGRADING SCHEDULE					
4. PERFORMING ORGANIZATION REPORT NUMBER(S) AFIT/GE/ENG/86J-1			5. MONITORING ORGANIZATION REPORT NUMBER(S)		
6a. NAME OF PERFORMING ORGANIZATION School of Engineering, Air Force Institute of Technology		6b. OFFICE SYMBOL (If applicable) AFIT/ENG		7a. NAME OF MONITORING ORGANIZATION	
6c. ADDRESS (City, State and ZIP Code) Wright-Patterson AFB, Ohio 45433			7b. ADDRESS (City, State and ZIP Code)		
8a. NAME OF FUNDING/SPONSORING ORGANIZATION Electromagnetic Sciences Division		8b. OFFICE SYMBOL (If applicable) RADC/EEAC		9. PROCUREMENT INSTRUMENT IDENTIFICATION NUMBER	
8c. ADDRESS (City, State and ZIP Code) Rome Air Development Center Hanscom AFB, MA 01731			10. SOURCE OF FUNDING NOS.		
			PROGRAM ELEMENT NO.	PROJECT NO.	TASK NO.
			WORK UNIT NO.		
11. TITLE (Include Security Classification) Investigation of Magnetostatic Surface Waves for Anisotropic Effects (Unclassified)					
12. PERSONAL AUTHOR(S) Robert E. Floyd					
13a. TYPE OF REPORT MS Thesis		13b. TIME COVERED FROM _____ TO _____		14. DATE OF REPORT (Yr., Mo., Day) 1986 June 2	
				15. PAGE COUNT 73	
16. SUPPLEMENTARY NOTATION <i>Approved for public release: DRW, AFM 100-1 E. E. WOLAVER Dean for Research and Professional Development Air Force Institute of Technology (AFIT) Wright-Patterson AFB, Ohio 45433</i>					
17. COSATI CODES			18. SUBJECT TERMS (Continue on reverse if necessary and identify by block number)		
FIELD	GROUP	SUB. GR.			
17	04, 09		magnetostatic; anisotropy; magnetostatic surface waves;		
09	01, 03		refraction; beam steering; magnetostatic delay line oscillator.		
19. ABSTRACT (Continue on reverse if necessary and identify by block number) A unique test apparatus was designed in order to investigate the effect of launching magnetostatic surface waves at different angles on a yttrium-iron-garnet (YIG) single crystal film. Many characteristics of the magnetostatic waves were measured, including amplitude, time delay, and beam steering. There was slight dependence of these characteristics on the launch angle. A second, more sensitive technique using the YIG films as delay lines in an oscillating circuit, was found to verify the influence of magnetocrystalline anisotropy on the magnetostatic surface wave. A calculated shift in frequency of the oscillator was found to be in agreement with previous calculations and measurements of anisotropic constants. In addition to these findings, an investigation of the influence of a metallization spaced closely to the propagation path was performed due to its influence on the above measurements. This metallization altered the velocity of the magnetostatic wave and demonstrated, for the first time, the refraction of a magnetostatic wave. This technique may prove useful for instantaneous frequency selection in electronic countermeasure equipment. Thesis Chairman: Roger D. Colvin, Capt USAF					
20. DISTRIBUTION/AVAILABILITY OF ABSTRACT UNCLASSIFIED/UNLIMITED <input checked="" type="checkbox"/> SAME AS RPT. <input type="checkbox"/> DTIC USERS <input type="checkbox"/>			21. ABSTRACT SECURITY CLASSIFICATION Unclassified		
22a. NAME OF RESPONSIBLE INDIVIDUAL Roger D. Colvin, Capt USAF			22b. TELEPHONE NUMBER (Include Area Code) (513) 255-3576		22c. OFFICE SYMBOL AFIT/ENG

END

1/1-S6

DTIC